



This is a repository copy of *Rapid mid-infrared spectral-timing with JWST: GRS 1915+105 during a MIR–bright and X-ray–obscured state*.

White Rose Research Online URL for this paper:

<https://eprints.whiterose.ac.uk/223598/>

Version: Published Version

Article:

Gandhi, P. orcid.org/0000-0003-3105-2615, Borowski, E.S. orcid.org/0009-0002-6989-1019, Byrom, J. et al. (44 more authors) (2025) Rapid mid-infrared spectral-timing with JWST: GRS 1915+105 during a MIR–bright and X-ray–obscured state. *Monthly Notices of the Royal Astronomical Society*, 537 (2). pp. 1385-1403. ISSN 0035-8711

<https://doi.org/10.1093/mnras/staf036>

Reuse

This article is distributed under the terms of the Creative Commons Attribution (CC BY) licence. This licence allows you to distribute, remix, tweak, and build upon the work, even commercially, as long as you credit the authors for the original work. More information and the full terms of the licence here:

<https://creativecommons.org/licenses/>








































Takedown

If you consider content in White Rose Research Online to be in breach of UK law, please notify us by emailing eprints@whiterose.ac.uk including the URL of the record and the reason for the withdrawal request.



eprints@whiterose.ac.uk
<https://eprints.whiterose.ac.uk/>

Rapid mid-infrared spectral timing with *JWST*: GRS 1915+105 during an MIR-bright and X-ray-obscured state

P. Gandhi ^{1,★}, E. S. Borowski ², J. Byrom,¹ R. I. Hynes ², T. J. Maccarone,³ A. W. Shaw ⁴, O. K. Adegoke ⁵, D. Altamirano ¹, M. C. Baglio ⁶, Y. Bhargava ⁷, C. T. Britt,⁸ D. A. H. Buckley ⁹, D. J. K. Buisson,[†] P. Casella ¹⁰, N. Castro Segura ¹¹, P. A. Charles,^{1,12} J. M. Corral-Santana ¹³, V. S. Dhillon ^{14,15}, R. Fender,¹² A. Gúrpide ¹, C. O. Heinke ¹⁶, A. B. Igl ², C. Knigge ¹, S. Markoff ¹⁷, G. Mastroserio ¹⁸, M. L. McCollough ¹⁹, M. Middleton ¹, J. M. Miller,²⁰ J. C. A. Miller-Jones ²¹, S. E. Motta ⁶, J. A. Paice ²², D. D. Pawar,²³ R. M. Plotkin ²⁴, P. Pradhan ²⁵, M. E. Ressler ²⁶, D. M. Russell ²⁷, T. D. Russell ²⁸, P. Santos-Sanz ²⁹, T. Shahbaz ^{15,30}, G. R. Sivakoff ¹⁶, D. Steeghs ¹¹, A. J. Tetarenko ³¹, J. A. Tomsick ³², F. M. Vincentelli ¹, M. George ¹, M. Gurwell ¹⁹ and R. Rao ¹⁹ (JWST Timing Consortium)

Affiliations are listed at the end of the paper

Accepted 2025 January 7. Received 2024 December 20; in original form 2024 June 21

ABSTRACT

We present mid-infrared (MIR) spectral-timing measurements of the prototypical Galactic microquasar GRS 1915+105. The source was observed with the Mid-Infrared Instrument (MIRI) onboard *JWST* in June 2023 at an MIR luminosity $L_{\text{MIR}} \approx 10^{36} \text{ erg s}^{-1}$ exceeding past infrared levels by about a factor of 10. In contrast, the X-ray flux is much fainter than the historical average, in the source’s now-persistent ‘obscured’ state. The MIRI low-resolution spectrum shows a plethora of emission lines, the strongest of which are consistent with recombination in the hydrogen Pfund (Pf) series and higher. Low-amplitude (~ 1 per cent) but highly significant peak-to-peak photometric variability is found on time-scales of ~ 1000 s. The brightest Pf(6–5) emission line lags the continuum. Though difficult to constrain accurately, this lag is commensurate with light-travel time-scales across the outer accretion disc or with expected recombination time-scales inferred from emission-line diagnostics. Using the emission line as a bolometric indicator suggests a moderate (~ 5 –30 per cent Eddington) intrinsic accretion rate. Multiwavelength monitoring shows that *JWST* caught the source close in time to unprecedentedly bright MIR and radio long-term flaring. Assuming a thermal bremsstrahlung origin for the MIRI continuum suggests an unsustainably high mass-loss rate during this time unless the wind remains bound, though other possible origins cannot be ruled out. Polycyclic aromatic hydrocarbon features previously detected with *Spitzer* are now less clear in the MIRI data, arguing for possible destruction of dust in the interim. These results provide a preview of new parameter space for exploring MIR spectral timing in X-ray binaries and other variable cosmic sources on rapid time-scales.

Key words: infrared: general – X-rays: binaries.

1 INTRODUCTION

X-ray binaries (XRBs) host a compact object, either a black hole or a neutron star, in a bound orbit with a secondary star from which matter is accreted. XRBs represent the endpoints of massive stellar evolution in binaries. Their compact sizes also make excellent laboratories for studying accretion as a rapid time-domain phenomenon, and there is now a rich heritage of observations studying their flux variations across a range of time-scales (e.g. Belloni 2010, and references

therein). Variability is also an important tool for disentangling emission from multiple physical components (e.g. the accretion disc, corona, jet, and donor star; van der Klis 1995; Markoff, Falcke & Fender 2001; Gandhi et al. 2011; Veledina, Poutanen & Vurm 2013; Malzac 2014 and references therein) that can overlap spectrally, and make studies of XRBs challenging.

GRS 1915+105 is the prototypical ‘microquasar’, displaying apparently superluminal relativistic jets and prolific X-ray variability patterns (Mirabel & Rodríguez 1994; Belloni et al. 2000). Continuum variability spanning a wide range of time-scales has been observed and found to be correlated across many wavelengths, interpreted as evidence for disc–jet coupling and plasma ejections on time-scales of ~ 30 min and longer (Fender et al. 1997; Eikenberry et al.

* E-mail: poshak.gandhi@soton.ac.uk

† Independent.

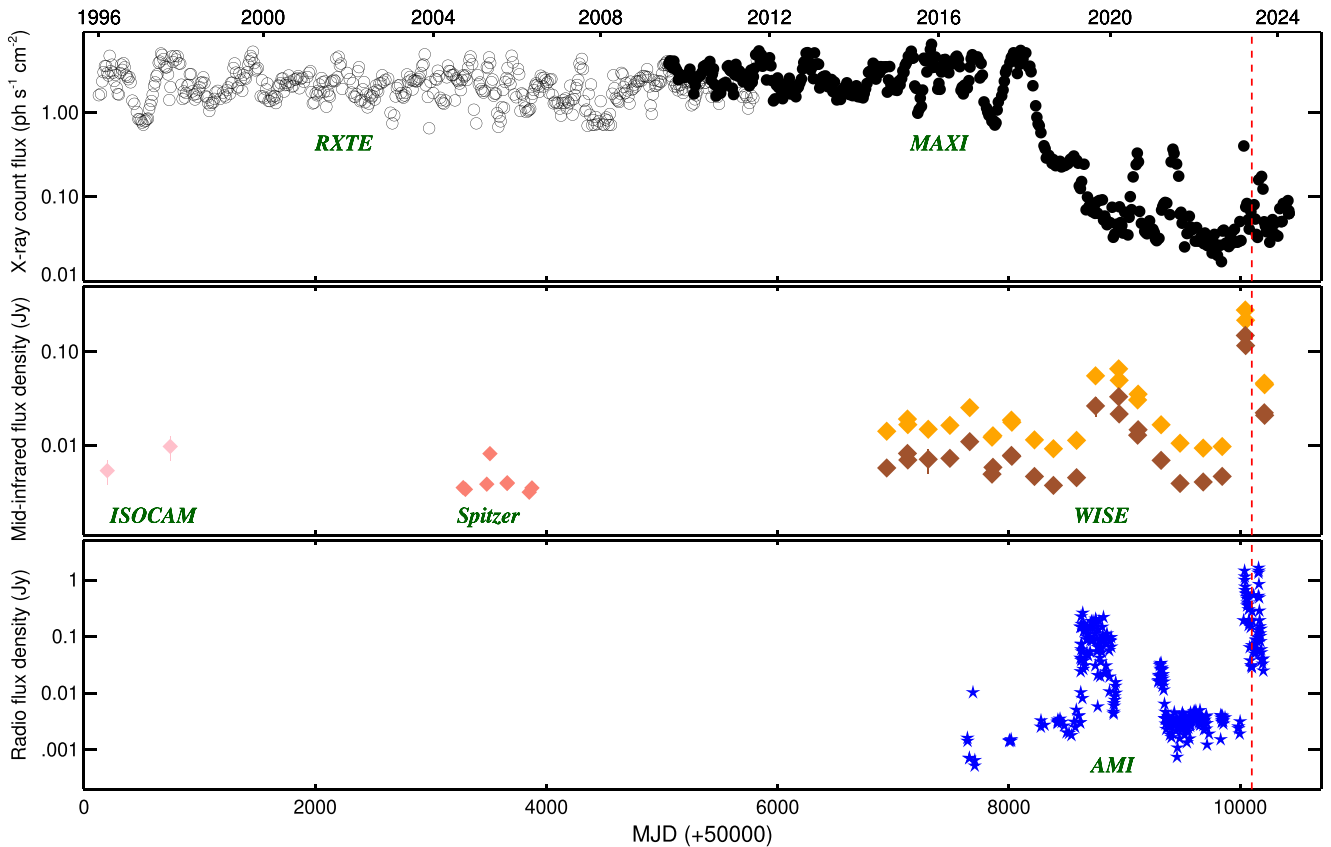


Figure 1. (Top) Long-term X-ray light-curve monitoring of GRS 1915+105 with MAXI (2–20 keV; filled circles) and *RXTE* All-Sky Monitor (ASM; 1.5–12 keV; unfilled circles). The *RXTE* count rates have been normalized to match the MAXI data at their peaks, simply in order to plot and compare them simultaneously. (Middle) Long-term MIR flux densities from Infrared Space Observatory Camera (ISOCAM; LW2 5–8.5 μm ; 1996–1997), *Spitzer* IRS 5–5.5 μm (2004–2006), and *NEOWISE* W1 (orange diamonds; shifted by $2\times$ for display purposes) and W2 (brown) light curves from 2014 onwards. (Bottom) Long-term AMI-LA radio light curve. Data are taken at 15 GHz. The *JWST* observation date (2023 June 6) is indicated by a vertical red line.

1998a; Mirabel et al. 1998; Rothstein, Eikenberry & Matthews 2005; Neilsen & Lee 2009; Ueda et al. 2010; Vincentelli et al. 2023). With an integrated Galactic reddening $E_{B-V} = 8.9 \pm 0.7$ mag along its line of sight (Schlafly & Finkbeiner 2011), the source is too extinguished for most optical observations. However, sub-minute near-infrared (NIR) continuum variability has also been observed to be correlated with X-rays (Lasso-Cabrera & Eikenberry 2013).

The source has been observed in the mid-infrared (MIR) with previous missions. Rahoui et al. (2010) reported a detailed analysis of *Spitzer* spectral observations, finding signatures of dust together with an irradiated accretion disc, with both components responding to the intrinsic X-ray variations over long time-scales of months (but see Harrison et al. 2014). Though no short-term emission-line variability study was reported from the *Spitzer* observations (perhaps because the integration times, typically about 30 min, did not sample the variability well), evidence for such variations has been reported in the NIR by Eikenberry et al. (1998b), who identified radiative pumping as the cause of common emission-line and continuum flux trends.

Since 2018, the source has also entered a new and puzzling spectral state, with the X-ray flux having systematically faded by a factor of 10–100 compared to its historical persistent average. None the less, there are multiple indications – from X-rays and radio monitoring, together with detection of NIR winds – that the source remains active and intrinsically luminous, with the faintness likely

resulting from enhanced obscuration (Negoro et al. 2018; Miller et al. 2020; Balakrishnan et al. 2021; Motta et al. 2021; Sánchez-Sierras et al. 2023a). The cause and nature of this ‘obscured’ state remain unclear, though a change in the outer disc geometry, triggering of multiwavelength winds, and/or a change in accretion rate have been proposed (Miller et al. 2020; Neilsen et al. 2020; Balakrishnan et al. 2021; Sánchez-Sierras et al. 2023a).

Fig. 1 shows the long-term multiwavelength behaviour of the source, including X-rays, radio, and MIR monitoring data. X-ray all-sky monitors (Bradt, Rothschild & Swank 1993; Levine et al. 1996; Matsuoka et al. 2009) show the systematic flux decline post-2018, with later emission dominated by a few flares reaching at most a factor of a few below previous fluxes. The middle panel shows long-term MIR measurements (in bands close together in wavelength centred around 3.4–8.5 μm) from the *Infrared Space Observatory* (*ISO*) mission (Cesarsky et al. 1996; Clegg et al. 1996; Kessler et al. 1996), *Spitzer* Infrared Spectrograph (IRS; Houck et al. 2004; Werner et al. 2004), and *NEOWISE* (*Near-Earth Object Wide-field Infrared Survey Explorer*; Wright et al. 2010; Mainzer et al. 2011) observations. Finally, the bottom panel shows Arcminute Microkelvin Imager – Long Array (AMI-LA; Zwart et al. 2008) 15 GHz radio monitoring since 2016. Both the radio and the MIR light curves show pronounced long-term flaring in recent years. Moreover, the *NEOWISE* data show flares during the obscured state reaching an order of magnitude brighter than historical MIR fluxes

Table 1. Physical parameters of GRS 1915+105 adopted in this work.

Distance d	9.4 ± 1.0 kpc
Orbital period P	33.85 ± 0.16 d
Black hole mass M_{BH}	$11.2 \pm 1.7 M_{\odot}$
Inclination i	64 ± 4 deg
Mass ratio $q(=M_2/M_1)$	0.042 ± 0.024
Binary separation a	232.2 ± 12.0 lt-sec
Roche lobe r_L/a	0.16 ± 0.03
Extinction A_V	19.2 ± 0.17 mag

during the X-ray-bright state – all indicators of an intrinsically active source.

Here, we present *JWST* MIR spectral timing of GRS 1915+105. A *JWST* observation was conducted close in-time to multiwavelength long-term flaring, which included an event of exceptional brightening in the radio and MIR (Fig. 1), presenting a unique opportunity to study the source in the MIR during its novel X-ray-obscured state. We aim to try and understand the origin of the MIR emission and shed light on the circumnuclear environment in this new state.

JWST was not designed as a dedicated timing observatory. None the less, its capabilities allow interesting new timing parameter space to be exploited, which we demonstrate here to study rapid (stochastic) accretion variability as a use case. This is the first in a series of papers dedicated to exploring MIR spectral timing for XRBs. The sensitivity of these data are orders of magnitude superior to previous MIR observations of the source, offering new possibilities in precision spectral-timing exploration.

A kinematic distance of 9.4 ± 0.6 (stat.) ± 0.8 (sys.) kpc to GRS 1915+105 has been estimated (Reid & Miller-Jones 2023), which is consistent with a radio parallax distance of $8.6^{+2.0}_{-1.6}$ kpc and yields a black hole mass of $M_{\text{BH}} = 11.2 M_{\odot}$ and a jet inclination of $i = 64 \pm 4$ deg (Reid et al. 2014). The secondary is an evolved K1/5 III star in a long orbit $P = 33.85 \pm 0.16$ d (Greiner et al. 2001; Steeghs et al. 2013). These and other adopted source parameters from Casares & Jonker (2014) are listed in Table 1. The adopted value of optical extinction from Chapuis & Corbel (2004) will be discussed later.

2 OBSERVATIONS

GRS 1915+105 was observed on 2023 June 6 using Mid-Infrared Instrument (MIRI; Rieke et al. 2015) in the slitless low-resolution spectroscopy (LRS) mode (Kendrew et al. 2015). This was a time-series observation (TSO) with a continuous stare on-target through the SLITLESS PRISM sub-array, with no dithering. The first on-source science frame started at UT 08:57:49.86. A separate work examines the absolute time accuracy of the mission clock (Shaw et al. 2025). Observations were performed in the standard non-destructive FASTR1 mode (cf. Ressler et al. 2015; Dyrek et al. 2024), with a series of individual frames (or ‘groups’), each 0.159 s in duration, combining charge on a ‘ramp’ to yield a cumulative ‘integration’. A total of $n_{\text{INT}} = 4150$ integrations were obtained, each comprising $n_{\text{GRP}} = 10$ science groups. The detector is reset at the end of each integration, resulting in a dead time of one group between successive integrations. The time of the final science frame was UT 10:58:48.44, yielding a full science observation of just over 2 h.

The data were processed through *JWST* pipeline version build 10.1, Calibration version 1.13.4. The pipeline itself comprises an elaborate set of intertwined stages and is still in the early (post-launch) stages of development. Its main stages are (1) detector level calibration,

(2) spectroscopic calibration, and (3) outlier detection and spectral extraction.

A number of inadequacies were identified in our run of the pipeline. Stage 1 was found to be overflagging pixels as bad. This is likely to be a result of the known ‘brighter-fatter’ effect of the MIRI detectors (Argyriou et al. 2023) and its handling in the current version of the pipeline (STScI, private communication). In consultation with the instrument team, we reprocessed the data through the pipeline by setting the `flag_4_neighbors` flag to be `false` and the `JUMP_rejection_threshold` to 15σ (from its default value of 4). Stage 3 of the pipeline was also found to be introducing substantial scatter between integrations in its outlier detection step, especially within the first few integrations when there is also a known detector settling delay. Again, in consultation with STScI and while this issue is investigated, we chose to forego the outlier detection step entirely. This ends up leaving a few residual artefacts that are not filtered out by the pipeline and need to be individually accounted for in later analysis (cf. Section 3.2), but should not impact the bulk of our analysis.

The spectral trace across all integrations was examined by eye and was found to be stable at the sub-pixel level throughout the observation. A rectangular aperture of width 5 pixels (0.55 arcsec) was used for spectral extraction. The pipeline automatically accounts for wavelength-dependent aperture flux losses. Background subtraction is not implemented by default for slitless observations. We used two rectangular source-free apertures (experimenting with 8–11 pixel widths) for computing and subtracting the background in each integration. During analysis of the source r.m.s. variability (discussed in Section 3), we found that the pipeline does not incorporate background uncertainties in its total extracted flux error, even when background subtraction is implemented (confirmed by STScI; private communication). We thus implemented a manual correction by extracting background flux errors and adding them in quadrature to the source flux errors, but we suspect that some uncertainties are still being underestimated at the red end of the MIRI wavelength range. This is discussed in Appendix A and could be related to known issues with read-noise subtraction, which should increasingly dominate the error budget at long wavelengths.¹ The bulk of our analysis herein should not be strongly impacted by these factors, except at the longest wavelengths, which we highlight in relevant places in the text later on.

We extract spectra across the full delivered wavelength range of 4.5–14 μm , though it should be noted that the primary calibrations for MIRI are best understood between ≈ 5 and 12 μm , and there remain uncertainties at longer wavelengths. Our data also become background-dominated above $\approx 13 \mu\text{m}$. In order to check the spectral calibration, we conducted a comparison of MIRI data obtained in an identical (LRS SLITLESS PRISM TSO) mode as part of a commissioning observation. These data, of the star L168–9b, showed very similar spectral features at the two wavelength ends of the spectrum, a clear indication of imperfect spectral calibration. We used these commissioning observations to obtain a wavelength-dependent spectral calibration correction, which was then applied to GRS 1915+105. The details of this procedure can be found in Appendix A. The correction factor introduces only small changes (\approx a few percent) over the bulk of the primary MIRI range, but becomes more important above 12 μm .

Finally, we note that the pipeline actually delivers source signal at wavelengths extending down to $\lambda \approx 4 \mu\text{m}$. However, there is a known

¹<https://jwst-docs.stsci.edu/deprecated-jdcox-articles/jwst-calibration-pipeline-caveats/jwst-miri-lrs-pipeline-caveats>

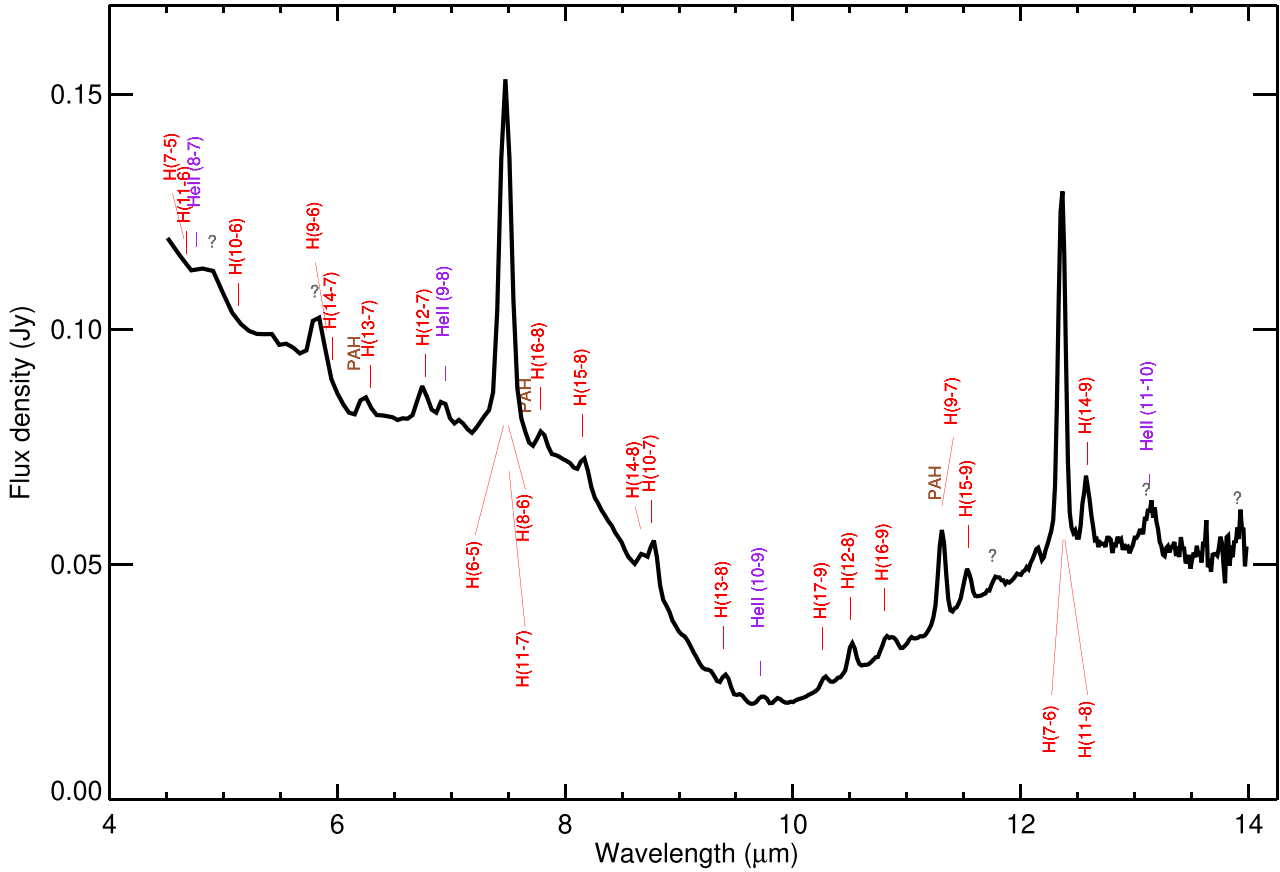


Figure 2. MIRI/LRS spectrum of GRS 1915+105. The annotated identifications are not meant to be complete. Furthermore, while some potential line identifications are listed, the low resolution precludes unambiguous identification in many cases.

spectral fold-over below $\approx 4.5 \mu\text{m}$ in slitless mode, so reflection and scattering cause longer wavelength light to contaminate detector regions characteristic of shorter wavelengths (Wright et al. 2023). We thus restrict our analysis to $\lambda > 4.5 \mu\text{m}$.

3 RESULTS

3.1 Spectroscopy

Fig. 2 shows the final average MIRI LRS spectrum of GRS 1915+105 across the entire wavelength range of 4.5–14 μm . A bright continuum is detected, peaking above a flux density $F_\nu \approx 100 \text{ mJy}$ at the short wavelength end ($\approx 5 \mu\text{m}$). A deep absorption feature is detected over $\approx 9\text{--}11 \mu\text{m}$, which can be attributed to silicates (see Section 4).

Many emission lines are detected, the most prominent of which are hydrogen recombination features from the Pfund (Pf; $n_l = 5$) and Humphrey (Hp; $n_l = 6$) series.² Potential identifications of many features are annotated in the figure. Several of these are strong and significant, given the high signal-to-noise ratio (S/N) of the data. However, in many instances, exact identification of features remains ambiguous, primarily due to the low spectral resolution (R) of the observing mode, which ranges from $R \approx 40$ ($\Delta\lambda = 0.125 \mu\text{m}$;

$\Delta v = 7500 \text{ km s}^{-1}$) near 5 μm to ≈ 160 ($\Delta\lambda = 0.063 \mu\text{m}$; $\Delta v = 2000 \text{ km s}^{-1}$) at 10 μm (Kendrew et al. 2015).

Interpretations of the rich emission-line spectrum and the continuum will be discussed shortly. Detailed line investigation (especially accounting for blending) is, however, beyond the scope of this work, and is likely to require higher spectral-resolution observations. Here, we present the results of basic line fitting to a few specific emission lines that will be discussed below.

Profile fits were carried out assuming a single Gaussian component atop a local linear (first-order) continuum. This allowed measurements of centroid wavelengths, full widths at half-maximum (FWHMs), and dereddened³ fluxes. These results can be found in Table 2.

There is no consistent pattern of centroid wavelength shifts from the most prominent expected line identifications, with the main uncertainty being possible confusion related to line blending. Regarding line widths, the measured FWHMs range over $\approx 0.073\text{--}0.115 \mu\text{m}$. The latter value is for the strongest feature peaking around $\lambda = 7.48 \mu\text{m}$ and consistent with H(Pf)(6–5). At this wavelength, the expected line width for an unresolved line is $\text{FWHM} = 0.075 \mu\text{m}$ ($R \approx 99.5$) based upon a linear fit to the spectral-resolution trace of Kendrew et al. (2015). Thus, this feature appears to be significantly resolved. If this can be attributed solely to a single emission line, the implied velocity width is $\Delta v \approx 3500 \text{ km s}^{-1}$.

²Appendix B presents a reference list of some of the key H and He II emission lines that lie in the MIRI range.

³Dereddening corrections are detailed in Section 4.1.

Table 2. Strong emission lines identified or discussed in the text body.

Wavelength of fit (μm)	FWHM (μm)	Dereddened flux ($\times 10^{-13} \text{ erg s}^{-1} \text{ cm}^{-2}$)	Potential identification
6.239 ± 0.004	0.096 ± 0.009	0.09 ± 0.04	PAH feature ~ 6.2
"	0.115 ± 0.001	10.03 ± 0.03	H (13–7) 6.2919 H Pf (6–5) 7.4599
7.4774 ± 0.0003			H Hp (8–6) 7.5025 H (11–7) 7.5081
"	0.08 ± 0.01	0.08 ± 0.01	PAH feature ~ 7.7 H (16–8) 7.7804
7.800 ± 0.005			He II (10–9) 9.7135
9.737 ± 0.005	$0.098^{+0.008}_{-0.006}$	0.18 ± 0.04	H (9–7) 11.3087 He I 11.3010 PAH feature ~ 11.3
11.307 ± 0.001	0.073 ± 0.001	0.62 ± 0.03	H Hp (7–6) 12.3719 H (11–8) 12.3871
"			
12.3602 ± 0.0006	0.074 ± 0.001	3.56 ± 0.09	
"			

Note. Fits based on single, symmetric Gaussian model parametrization of the lines. Only the most prominent lines and those discussed specifically in the text are listed here. Ambiguous possible line identifications (which may not be complete) are listed in the final column, with wavelengths stated in μm .

By comparison, emission lines as broad as 2100 km s^{-1} have been recently observed in the *NIR* in this source (Sánchez-Sierras et al. 2023a). The main systematic uncertainty here remains our inability to deblend the various possible emission lines that may overlap and artificially broaden single-component fits.

3.2 Timing

3.2.1 General properties

The desire for timing analysis motivated our original choice of the MIRI slitless LRS mode (Kendrew et al. 2018) for this observation. The data are collated in three-dimensional ‘cubes’ comprising two-dimensional spectral images sampled at each integration. As a starting point to investigate the timing properties, the spectral-timing cubes can be summed over the full wavelength range to produce light curves in desired wavelength ranges. Fig. 3 shows such light curves spanning short to long wavelength ranges, together with a ‘white-light’ time series summed over the full nominal MIRI range of 4.5–12 micron.

As a result of the high source brightness, the typical cumulative S/N ratio in each 1.59 s integration of the white-light data is ≈ 700 . This allows fine sensitivity to temporal flux variations, revealing weak (\sim per cent level) but significant fluctuations. A few obvious, but minor, artefacts remain in the light curve (e.g. the spike in the initial integrations and the cosmic rays near 7000 s), and are related to pipeline shortcomings (cf. Section 2). These do not impact our inferences below.

For the white-light data, we find an excess r.m.s. of 1.1 per cent above statistical errors, defined as

$$\text{r.m.s.}_\lambda = \frac{\sqrt{\text{var}_\lambda - \sigma_{\text{err}(\lambda)}^2}}{\bar{f}_\lambda}, \quad (1)$$

where \bar{f} denotes the mean flux of the light curve, var is its raw variance, σ_{err} represents the individual measurement errors, and σ_{err}^2 is the mean square error (cf. Vaughan et al. 2003). All quantities above are functions of wavelength λ .

The strongest (peak-to-peak) variations occur on time-scales of ~ 1000 – 2000 s, and there are no obvious characteristic faster time-scales. This was confirmed by computing the power spectral density (PSD) of the white-light time series, displayed in Fig. 4. This represents the squared modulus of the complex-valued Fourier spectrum of the light curve, and is normalized according to the r.m.s. of the light curve (cf. Belloni & Hasinger 1990; Vaughan et al. 2003). The PSD was accumulated in three time segments, each 2048 s in length, which were then averaged to compute the mean and scatter. A light binning by a factor of 1.1 in logarithmic frequency bins has been applied. The PSD peaks at low frequencies, showing a steep fall from frequencies of ≈ 0.0005 to ≈ 0.05 Hz, above which white noise starts to dominate. The effect of dead time has not been corrected for in this PSD analysis, but its impact should be minimal given the short duration of the gap between integrations and the weakness of any rapid variations. The slope of the steep component is consistent with a simple red-noise power law $P_\nu \propto \nu^{-\alpha}$, with $\alpha = -2.3 \pm 0.05$.

Investigating the typical variability as a function of wavelength, it can be seen from Fig. 3 that the mean trace of the light curves in all wavelength ranges is very similar in terms of shape and peak-to-peak variability. However, the longer wavelengths above $10 \mu\text{m}$ also show substantial excess scatter around the instantaneous mean. This was confirmed through a wavelength-resolved r.m.s. plot, which also showed the same trend. This rise in variability at the longer wavelengths is a suspected artefact of the aforementioned underestimation of uncertainties at the red end (cf. Section 2), and we do not consider it to be real.

At the wavelengths of many of the strong emission lines, the r.m.s. was found to be depressed. An exception in this regard was He II (10–9) $\lambda 9.7 \mu\text{m}$, where the r.m.s. was *enhanced* relative to the continuum. A figure showing the wavelength-dependent r.m.s. is presented in Appendix A where relevant pipeline artefacts are also detailed.

3.2.2 Timing: an emission-line time lag

We next searched for time lags in various spectral features. Light curves in the emission lines were found to show a similar variability

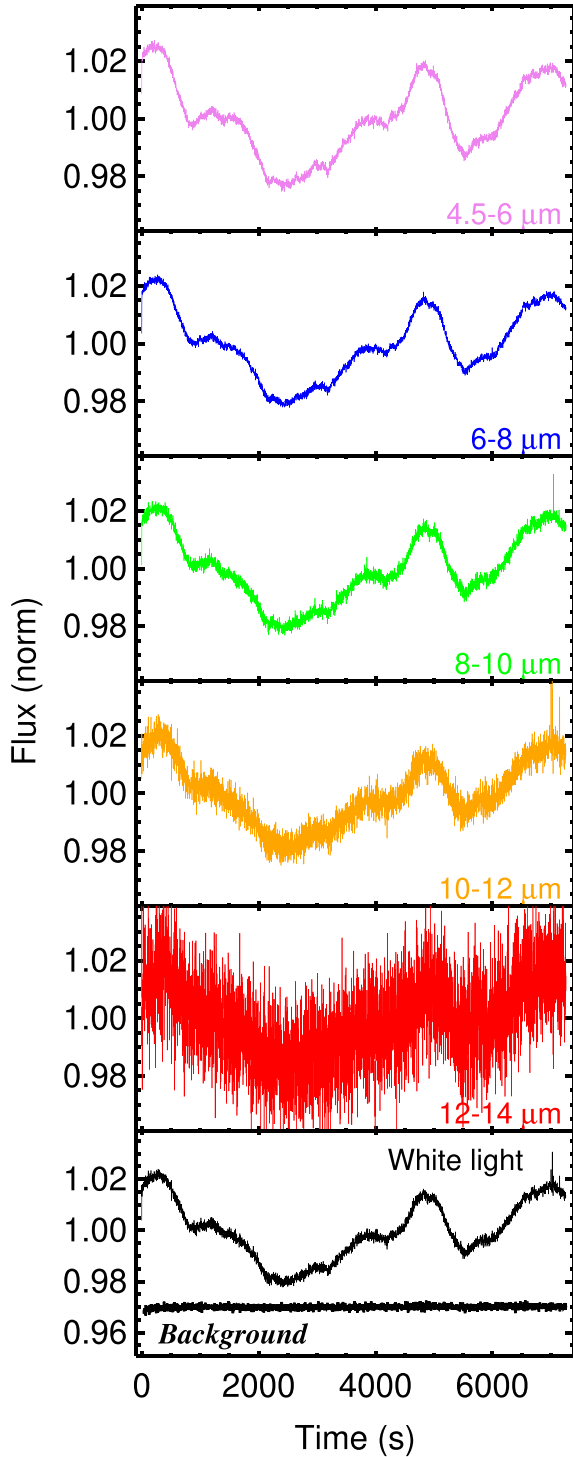


Figure 3. Multiwavelength time series of all 4150 integrations, split into annotated wavelength bins and normalized to the mean in each case. The spikes in the initial few integrations and also around a time of 7000 s are artificial features that have not been filtered out by the pipeline and should be ignored (they do not affect our lag analysis). The enhanced noise in the red filters is immediately apparent and is also an artefact of the pipeline (discussed in Section 2 and in Appendix A). The bottom panel reports the ‘white-light’ curve accumulated by the pipeline over 4.5–12 μm . The background light curve in the same band and units is also plotted, with an arbitrary offset applied on the y-axis in order to fit within the panel.

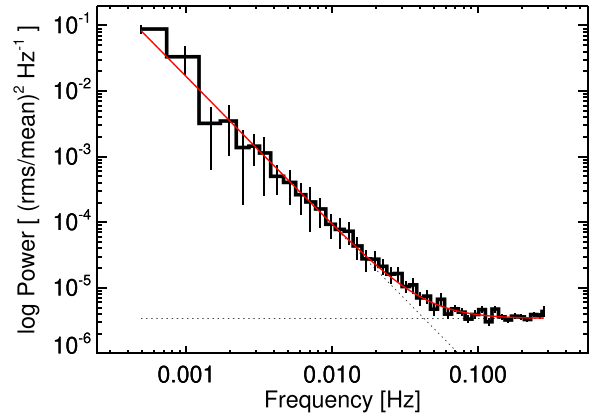


Figure 4. Power spectrum in white light, with the best-fitting power law of slope -2.3 overplotted, together with the constant white noise level.

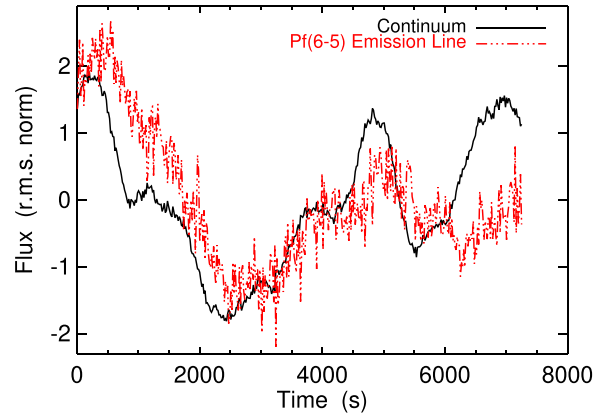


Figure 5. H P f(6–5) line (7.35–7.59 μm) and adjacent continuum (7–7.25 μm) light curves, binned by a factor of 10, mean-subtracted, and scaled by the respective scatter in each for cross-comparison.

pattern to the white-light data. Fig. 5 illustrates this with (i) a continuum-subtracted light curve aggregated over the strongest emission line Pf(6–5) $\lambda 7.35\text{--}7.59\ \mu\text{m}$ and (ii) the adjoining line-free continuum region (7–7.25 μm). These have lower S/N than the white-light curve in Fig. 5, as expected given their narrow wavelength span, but match the white-light profile well otherwise.

Evident to the eye is an indication of a possible delay in the emission line relative to the continuum. In order to quantify this, we undertook a detailed timing analysis of the two light curves.

We began by computing cross-correlation functions (CCFs), which quantify the strength of linear correlation between two time-series data sets, allowing for a relative lag (cf. Gandhi et al. 2010). Fig. 6 shows CCFs between the 7 μm continuum and the strongest Pf(6–5) line. The results are shown using the full light curves, as well as shorter independent time segments. In general, the correlations are strong, and consistently show a central peak lying at positive emission-line lags (with an associated delay $\approx 50\text{--}300\ \text{s}$ following the continuum), though the broad width of the peak makes it difficult to constrain the lag well. One time segment also shows a peak different from the others (the orange curve in the figure with the weakest CCF strength). This refers to the final $\approx 30\ \text{min}$ of data, when the emission-line response weakens substantially (cf. Fig. 5); we will return to this weakening of the response shortly.

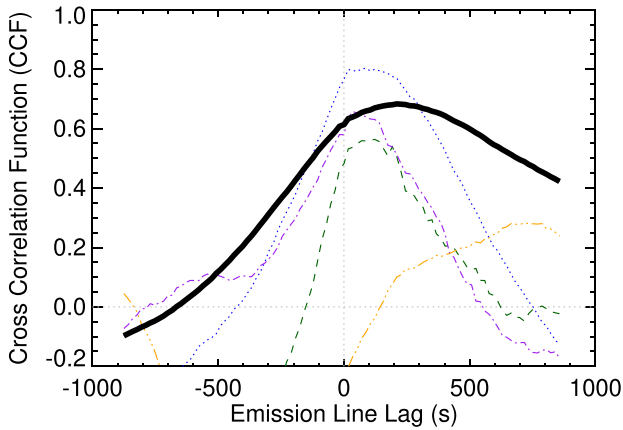


Figure 6. Cross-correlations between the continuum and the Pf (6–5) line. The thick black line refers to the full light curve, and the four thin broken curves denote the CCFs for four consecutive and independent time segments each approximately 1800 s long. A positive value of the lag on the x -axis implies the Pf line lagging the continuum.

In order to model and constrain the lag better, we next attempted transfer function modelling. Many works have demonstrated the effectiveness of such an approach for timing analyses of active galactic nuclei (AGNs) as well as XRBs (e.g. Peterson 1993; Hynes et al. 1998; Zu, Kochanek & Peterson 2011). This method takes a driving input light curve $\mathcal{I}(t)$ and convolves it through a transfer function $\Phi(t)$ to predict the smeared and lagged output time series $\mathcal{O}(t)$:

$$\mathcal{O}(t) = N \int \mathcal{I}(t') \Phi(t - t') dt'. \quad (2)$$

Here, N is a normalizing factor, which is a constant for stationary time series. For our purposes, the continuum is the driver input light curve $\mathcal{I}(t)$, and the model output $\mathcal{O}(t)$ is an estimator of the observed emission-line light curve. In practice, as we will discuss below, this model is probably too simplistic by itself, and requires additional complexities such as a transfer function that evolves with time.

We present results under the assumption of a Gaussian transfer function, which allows for a characteristic lag (τ) together with a smearing length (σ) of the continuum light curve as it is reprocessed in some extended medium. For the purposes of aiding the reader, one may imagine τ as representing a mean time lag due to light-travel or other ionic physical processes within a gaseous shell surrounding the source, and σ representing the physical extent of such a shell:

$$\Phi(t') = \frac{1}{\sqrt{2\pi}\sigma} e^{-\left(\frac{t'-\tau}{2\sigma}\right)^2}. \quad (3)$$

Numerically, the transfer function is represented by a kernel of finite length, and we found consistent results for kernels ranging between 500 and 1000 time bins.

Parameter estimation was carried out through a maximum likelihood (ML) technique. This computes the log-likelihood that the observed time-series fluxes can be jointly reproduced by the transfer function model. In practice, the negative log-likelihood is minimized, and then sampled through a Markov chain Monte Carlo (MCMC) sampling code, for which we utilized EMCEE (Foreman-Mackey et al. 2019) with 32 walkers, 5000 samples, and a burn-in period of 200. Constraints on the model parameters are implemented through the

use of uniform prior probabilities, which modulate the likelihood functions. Specifically, negative values of τ and σ were disallowed.⁴

We initially found that the above model did not produce an acceptable fit because of the aforementioned diminishing emission-line response with time, becoming substantially weaker, together with a diminishing CCF strength, towards the end of the observation (cf. Figs 5 and 6). This could be accounted for with a simple modification, making the normalization factor N time-variable, $N \equiv N(t)$. An exponentially diminishing dependence was found to be sufficient to first order: $N(t) = e^{-t/\tau_{\text{abs}}}$. The need for this parameter suggests that the time-series response is non-trivial, either non-linear or non-stationary, and we will also discuss possible interpretations of τ_{abs} below.

The results are shown in Fig. 7, which plots a binned version of the respective light curves for display purposes, overlaid with several MC samples around the best modelled response. The model reproduces the overall shape of the emission-line light curve well beyond ≈ 700 s. Earlier times cannot be modelled because of the finite length of the convolution kernel, which means that reproducing the initial portion of the light curve would require knowledge of the driving input continuum before the start of our observation.

The mean lag τ is found to be $1.5 (\pm 0.1) \times 10^2$ s, with the quoted uncertainties being the 16th and 84th percentiles of the marginalized sample. There is a strong degeneracy between τ and σ , the best fit for the latter centring around $4.5_{-0.8}^{+0.6} \times 10^2$ s. This degeneracy is a result of the short duration of our observation probing only a few distinct features and peak-to-peak cycles in the light curve. In other words, there are insufficient handles in our sampled data set to distinguish between lagging and smearing effects, which can qualitatively mimic each other.

The final free parameter τ_{abs} is fitted to be $5.2 (\pm 0.2) \times 10^3$ s. In the light curves shown in Fig. 7, it is apparent that the magnitude of the emission-line flux variations diminishes on such a time-scale, relative to those seen in the continuum. This parameter still fails to perfectly replicate the variations on the longest time-scales, with the models overpredicting the data beyond ≈ 5500 s, though the overall shape and lags appear to be well reproduced. Interpretations of τ_{abs} include a change in the emission-line response caused by patchy and changing absorption (as was also inferred in the XRB V404 Cyg; Motta et al. 2017; Walton et al. 2017). Specifically, if obscuration between the nucleus and the emission-line region increases over the course of the MIRI observation, this could manifest as an increasing optical depth that we parametrize as τ_{abs} . Alternatively, there could have been a systemic change in the source variability at late times, with the lag itself lengthening in a non-stationary manner towards the end of our observation. Finally, we cannot rule out the more mundane possibility that τ_{abs} may simply be a ‘fudge’ factor required by our current limited sampling of the observed time series. Irrespective of how they are interpreted, changes manifesting as τ_{abs} ultimately limit the precision with which we can measure any true lag, and thus also limit our ability to constrain the nature and extent of the emitting medium; this will be further discussed in Section 4.9.

Most other emission lines did not reveal any significant lag due to their comparative faintness. The only other emission line to show weak evidence for a lag was the Hp (7–6) line, which should dominate the next strongest observed line feature near $12.4 \mu\text{m}$. In this case, we found $\tau = 104_{-73}^{+86}$ s, $\sigma = 213_{-84}^{+79}$ s, and $\tau_{\text{abs}} = 6.5_{-0.6}^{+0.5} \times 10^3$ s. This is qualitatively consistent with the results from the Pf line (including

⁴We disallowed $\sigma \leq 1$ s to ensure that the transfer function remains numerically tractable over all reasonable parameter ranges.

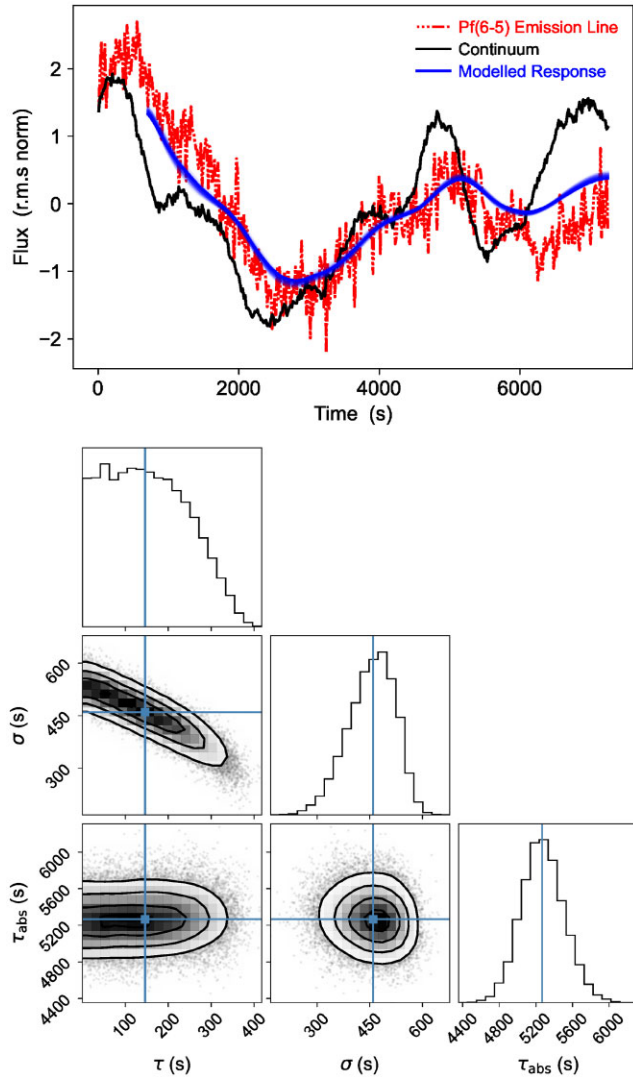


Figure 7. Results from the MCMC lag fitting. (Top) Emission-line light curve (red), continuum light curve (black), and the smeared and delayed response of the continuum curve (blue; 100 randomly chosen best-fitting samples). (Bottom) Corner plot, showing the distribution of fitted convolution parameters τ (mean lag), σ (smearing width), and the factor characterizing the time-scale over which the response becomes non-stationary (τ_{abs}).

the degeneracy between τ and σ), but with a shorter smearing length by a factor of about 2. The increased r.m.s. in the red region of the spectrum (Section 2) almost certainly impacts accurate estimation of uncertainties for this line.

4 DISCUSSION

4.1 Mid-infrared luminosity

The observed MIRI continuum is at a flux density $F_\nu \approx 70$ mJy at $8 \mu\text{m}$, corresponding to a monochromatic MIR luminosity $\lambda L_{\lambda(8 \mu\text{m})} = 2.8 (\pm 0.7) \times 10^{35} \text{ erg s}^{-1}$, or an integrated luminosity over the full MIRI spectral range of $L_{4-14} = 4.1 \times 10^{35} \text{ erg s}^{-1}$.

The optical extinction to GRS 1915+105 has been estimated by Chapuis & Corbel (2004) based upon CO observations of interstellar molecular clouds along the line of sight and assuming standard conversions between CO and H column densities' observations

(Rodríguez et al. 1995; Strong & Mattox 1996), together with known correlations between interstellar visual extinction and X-ray dust scattering optical depth (Predehl & Schmitt 1995). The estimated interstellar extinction is $A_V = 19.6 \pm 1.7 \text{ mag}$, which can be used to deredden the observed spectrum, if an extinction curve spanning the optical to MIR wavelength range is known. To achieve this, we follow Rahoui et al. (2010), who combined a standard selective extinction $R_V = 3.1 \text{ mag}$ value with the optical–NIR (Fitzpatrick & Massa 2009) and NIR–MIR (Chiar & Tielens 2006) extinction curves. The resultant A_λ/A_V values covering the MIRI spectral range are listed in Appendix C. For reference, $A_8 = 0.8 \text{ mag}$ at $8 \mu\text{m}$, and MIR extinction peaks around $A_{10} \approx 2.1 \text{ mag}$ within the silicate absorption feature.

Applying these extinction corrections results in an integrated intrinsic luminosity $L_{4-14}^{\text{int}} = 1.1 \times 10^{36} \text{ erg s}^{-1}$. The Eddington luminosity of the source for radiation impinging on ionized gas is $L_{\text{Edd}} = 1.4 \times 10^{39} \text{ erg s}^{-1}$, using $M_{\text{BH}} = 11.2 M_\odot$ (Table 1). So, a significant fraction $L_{4-14}^{\text{int}}/L_{\text{Edd}} = 7 \times 10^{-4}$ of the Eddington power is being radiated in the MIRI spectral range during our observations.

Correcting the entire MIRI range for extinction with the above prescription will effectively correct the curvature arising from silicate absorption. This is shown in Fig. 8, where several dereddened spectra are plotted together with an average dereddened spectrum (assuming a range of extinction values, sampled assuming a normal distribution using the known A_V uncertainty). We discuss the shape of this intrinsic spectrum below.

Previous MIR spectral observations of the source have included several by the *Spitzer* mission (Werner et al. 2004), with the source being detected by the IRS instrument (Houck et al. 2004) during eight observations spanning the years 2004–2006. Their detailed analysis has been published by Rahoui et al. (2010), and three representative epochs are plotted in Fig. 8. These were downloaded from the *Spitzer* IRS Enhanced Products archive, which provides background-subtracted, flux-calibrated, and merged spectra for each observation epoch.⁵

The continuum profiles of all the IRS spectra approximately match the MIRI data, albeit with much lower S/N. The median observed IRS flux density was 4 mJy with all the historical flux levels being nearly identical, except for one epoch on MJD 53851.41175 when the source was found to be closer to 7 mJy (this is the brightest *Spitzer* epoch shown in Fig. 8). Going further back, the mean flux of the source when it was observed photometrically in 1996–1997 with the *ISO* mission was ~ 5 – 10 mJy (Fuchs, Mirabel & Claret 2003), very similar to the *Spitzer* era. By contrast, the median flux observed with *JWST* in 2023 is close to 50 mJy, a factor of ≈ 5 – $13 \times$ brighter than historical values. We will discuss the implications of these long-term changes in Section 4.9.

4.2 Narrow emission lines

In Fig. 9, several model spectra are overplotted together with our median dereddened source spectrum. The models are recombination line spectra for H and He, for a range of annotated temperatures ($T = 10\,000$ – $20\,000 \text{ K}$) and densities ($n_{\text{H}} = 10^3$ – 10^8 cm^{-3}). The spectra were produced with the NEBULAR code (Schirmer 2016), assuming Case B recombination and 10 percent He abundance by part. The models have been convolved with a Gaussian kernel of

⁵<https://irsa.ipac.caltech.edu/data/SPITZER/docs/irs/irsinstrumenthandbook/84>

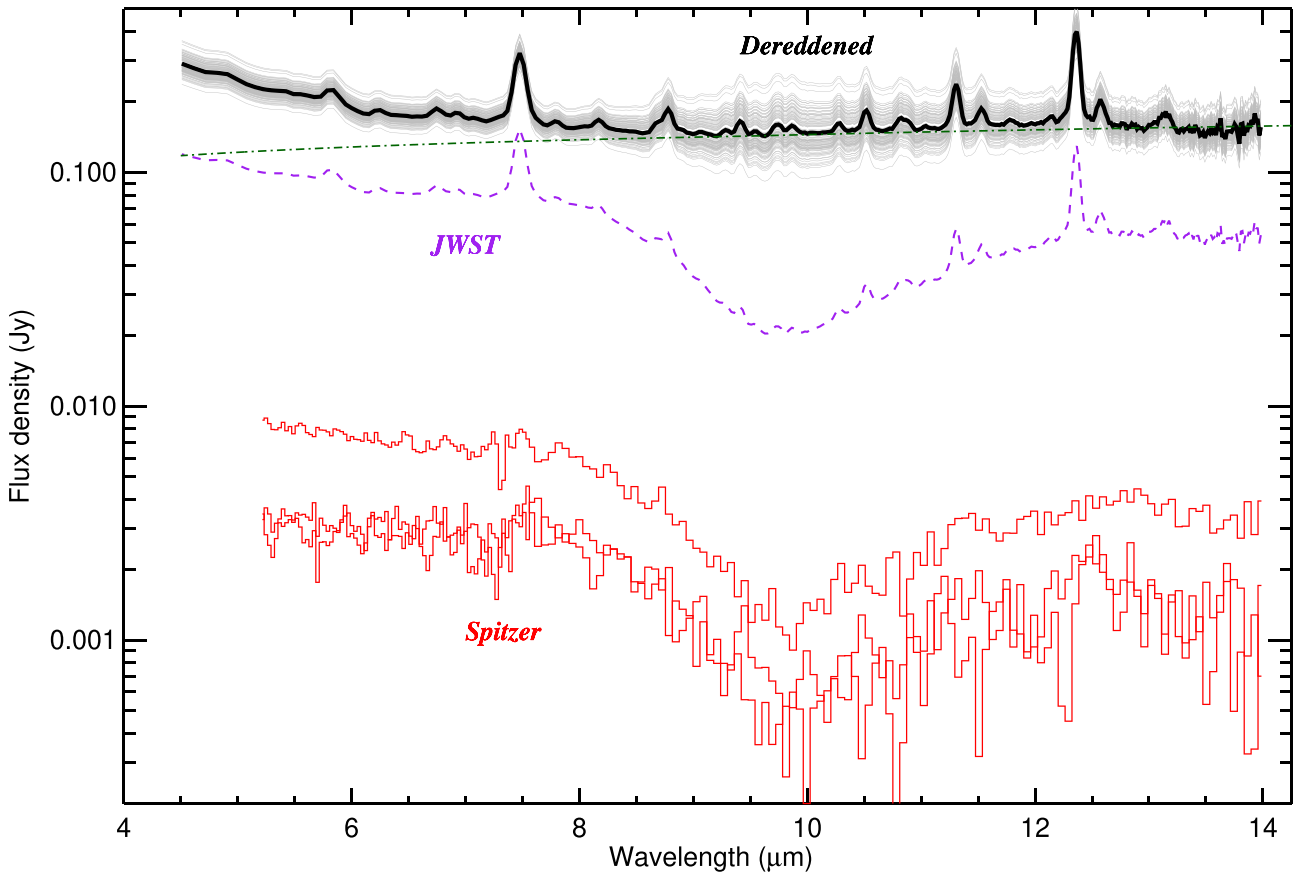


Figure 8. The observed MIRI/LRS spectrum of GRS 1915+105 in dashed purple, shown together with dereddened spectra (top), and three archival *Spitzer*/IRS observed spectra (bottom red) from MJD 53851.4117545, 53511.6928638, and 53299.219684. The spectra in grey have been dereddened assuming ISM A_V values sampled from a normal distribution with mean 19.6 mag and dispersion 1.7 mag. The thick black curve represents the mean intrinsic spectrum corrected for ISM extinction. The green dot-dashed curve represents an example thermal bremsstrahlung scenario for the continuum (Section 4.5.3).

spectral resolution, changing with wavelength according to Kendrew et al. (2015) in order to approximate the unresolved line widths as seen by MIRI.

The most immediate result apparent to the eye is that many of the emission lines, especially the strongest ones, are consistent with simple high-order H recombination transitions of the Pf ($n_l = 5$), Hp ($n_l = 6$), and higher series, up to $n_l = 8$ at least. While it is clear even to the eye that the relative model line ratios of many of the strongest lines approximate those seen in the data, it is worth emphasizing again that the low spectral resolution results in overlapping line associations, thus precluding robust identification in many cases. So, all of our line identifications and inferred flux measurements of individual features should be treated with some caution. A follow-up MIRI medium-resolution spectrum (MRS) mode should be able to resolve many of these degenerate identifications.

Several emission features with no current identification are also annotated therein. Some of these have potential matches with He I transitions found in the linelist of Chatzikos et al. (2023), but typically only at very high excitation, so we have not included them herein. NEBULAR does not include He I transitions in the MIRI wavelength range.

The location and nature of the line-forming region are currently unknown, but the model spectra allow a constraint on temperature under the assumption of Case B recombination. Specifically, high temperatures $T \gtrsim 20\,000$ K in the MIR line emission region are

excluded by the absence of prominent He II emission lines; cf. the strong prediction in the case of He II (10–9) feature at $9.7\ \mu\text{m}$, which we do not see. There is a weak nearby feature present in the data ($\lambda = 9.735\ \mu\text{m}$), which, if associated with He II (10–9), together with a similar possible identification of He II (9–8) $\lambda 6.9\ \mu\text{m}$ would be consistent with a temperature of $T \approx 17\,000$ K or lower. Though these recombination models provide surprisingly good qualitative descriptions of the data, it should be kept in mind that the XRB environment is likely more complex, and subject to the effects of a strongly accreting central engine. We touch upon more realistic photoionization simulations in Section 4.8.

4.3 Dust features

Spectral line indicators for the presence of dust include broad emission bands, such as polycyclic aromatic hydrocarbons (PAHs), which comprise large carbonaceous molecules and are commonly found in the interstellar medium (ISM), in star-forming galaxies and around AGN (e.g. Allamandola, Tielens & Barker 1989; Esquej et al. 2014). Vibrational modes in these molecules can be excited by ultraviolet (UV) radiation, which then results in infrared (IR) emission. There are several bands expected in the MIRI range – around 6.2 , 7.7 , and $11.3\ \mu\text{m}$, in particular. The centroid wavelengths and profile shapes of these features can vary depending upon the size and ionization state of the molecules present.

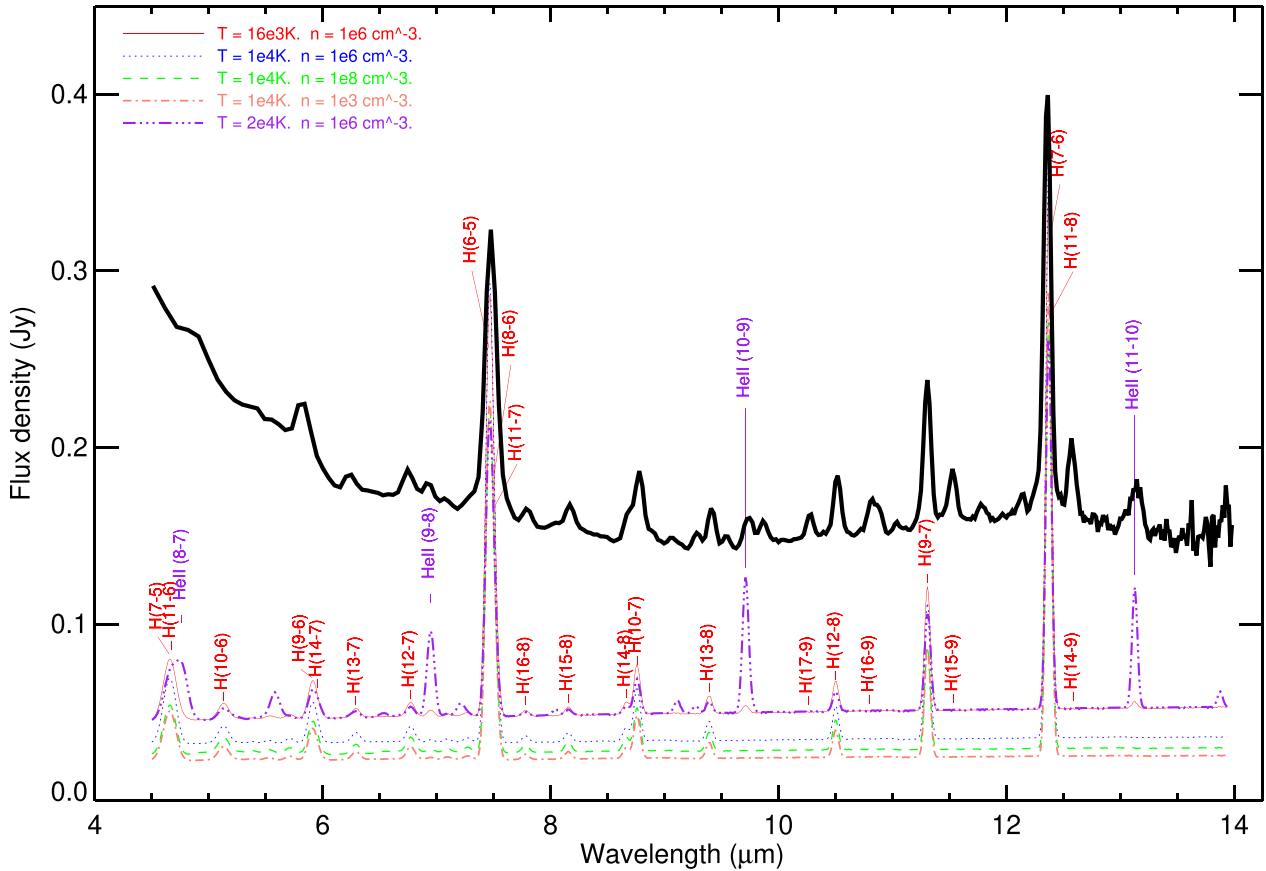


Figure 9. MIRI/LRS dereddened spectrum of GRS 1915+105 compared to several NEBULAR model spectra with annotated temperatures (in K) and densities (cm^{-3}).

Detection of these features in the MIRI spectrum is complicated by the low spectral resolution of our data. Around all three wavelengths, there are H recombination lines – H(13–7), H(16–8), and H(9–7), respectively, that could cause confusion. The emission feature at $11.3\ \mu\text{m}$ is the strongest of these, and its flux ratio relative to the other lines suggests that it is dominated by H(9–7) $\lambda 11.303\ \mu\text{m}$ recombination. PAH features are also thought to be destroyed in bright X-ray-dominated regions (Voit 1992), and as we discuss later, GRS 1915+105 probably remains in an intrinsically active and luminous state.

For all the reasons above, we are cautious of claiming detection of PAH features in the MIRI spectrum. Their detection was claimed by Rahoui et al. (2010) in the IRS data, where the recombination lines were also weaker. Their report of PAH features during the *Spitzer* epochs is thus more reliable. The *Spitzer* spectra have been further analysed by Harrison et al. (2014), who confirmed the presence of PAHs, though they highlighted that these features need not necessarily originate in close proximity to the source.

Analysing the fluxes of the putative PAH features in the MIRI spectra, we find that the flux of the emission line at $7.8\ \mu\text{m}$ [which could potentially be PAH 7.7 or could be H(16–8) instead] is very similar to that reported by Rahoui et al. (2010). If this really is attributable to PAHs, then it would require a steady PAH flux since ~ 2004 , despite the dramatic change in continuum flux. However, we also highlight the fact that all the strongest MIRI emissions lines and any lines near expected PAH wavelengths are narrow ($\text{FWHM} < 0.1\ \mu\text{m}$; cf. Table 2). By contrast, PAHs are generally measured to be significantly

broader ($\text{FWHM} > 0.1\text{--}0.2\ \mu\text{m}$) and often with skewed profiles, even in low S/N data sets (e.g. Allamandola et al. 1989; Rahoui et al. 2010; Armus et al. 2023), arguing that all of the relevant MIRI features are instead better explained as ionic (gas) recombination lines.

We thus rule out any substantial brightening of PAHs since the *Spitzer* observations in 2004–2006, with our data suggesting that PAHs may have since even been *destroyed*, presumably due to a change in the ionizing conditions of the PAH emission region. If so, not only does this place the site of the PAHs to be the vicinity of GRS 1915+105, it also sets a conservative upper limit of $\approx 17\ \text{yr}$ for the dust destruction time-scale. An MRS observation will be able to provide a more sensitive test of this hypothesis by helping to cleanly deconvolve the recombination lines.

Additional weak and broad unidentified IR bands are often taken to be signatures of the presence of dust (Chiar & Tielens 2006). Our dereddened spectrum is not perfectly flat (Fig. 9), and we cannot rule out the presence of such broad features (e.g. around $12\ \mu\text{m}$).

4.4 Timing

JWST's high sensitivity has enabled the detection of low-amplitude, but significant, flux variations of the order of 1 per cent (Fig. 3). Any characteristic variations in the light curves are on long time-scales ($\gtrsim 1000\ \text{s}$, at least), and the corresponding PSD rises steeply to low frequencies. Steep red-noise PSDs with slopes approaching $\beta = -2$ are rare in XRBs, but have been observed in a few other sources, e.g. during the bright 2015 outburst of V404 Cyg in the

optical (Gandhi et al. 2016). Such long time-scales exceed the light-travel time across the systems in both cases, and appear more akin to accretion-induced variations. Both V404 Cyg and GRS 1915+105 were probably also observed at relatively high L/L_{Edd} , though variability and obscuration render bolometric luminosity measurements difficult (cf. Section 4.8).

The emission-line lag that we find is also exceptionally long. Studies of reprocessing in XRBs have focused on the inner accretion zones – either the accretion disc or inner jet (e.g. Hynes et al. 2003; Gandhi et al. 2008, 2010; Casella et al. 2010; Paice et al. 2019; Vincentelli et al. 2019; Tetarenko et al. 2021), or on the companion star (O’Brien et al. 2002; Muñoz-Darias et al. 2007), where characteristic lags are of the order of seconds. Short NIR continuum lags with respect to X-rays have also been found in GRS 1915+105 (Lasso-Cabrera & Eikenberry 2013). Common patterns of X-ray and NIR rise and decoupling of flares on time-scales of ~ 30 min were found in the early days of multiwavelength follow-up of the source, and ascribed to synchrotron plasma ejecta (Eikenberry et al. 1998a; Mirabel et al. 1998). With regard to the emission lines specifically, continuum and line flux correlations were identified in the NIR by Eikenberry et al. (1998b) and interpreted as evidence for radiative line pumping, though no lags could be identified in those data.

Our direct measurement of an emission-line lag is the first such evidence of MIR line flux ‘reverberation’ in an XRB, to our knowledge. The mean lag that we measure is $\tau \approx 150$ s, but there is strong degeneracy with the smearing time-scale kernel, which is a factor of ≈ 3 longer. Moreover, the transfer function itself appears to be non-stationary in time (Section 3.2). All of this impacts our ability to pin down the exact lag in our data set, though it is nevertheless consistent with being several hundred seconds. A modestly longer observation probing a few additional flux rise and fall cycles should be able to determine the lag robustly.

The line–continuum correlation that we observe does not necessarily imply a causal relationship. Instead, it is likely that both the MIR continuum and lines are driven by higher energy UV and X-ray radiation from the central source. If one wishes to determine the true lag of the emission lines with respect to the central high-energy radiation, an *additional* lag related to the light-travel time from the nucleus will need to be included. If the MIR originates near the outer accretion disc extending close to the Roche lobe of the secondary star, this additional lag will be of the order of 200 s (cf. Table 1).

Furthermore, any finite recombination times will also introduce time delays, further complicating the interpretation of the lags. In order to evaluate this, we need a constraint on the gas density, which we turn to next.

4.5 The gas density

Constraining the gas density n_{H} is key to determining the nature of the source of MIR emission. Here, we consider four complementary estimates on n_{H} and what we can learn from these independent considerations. It is worth bearing in mind that all are subject to the caveat that we are likely only probing the optically thin portion of the emitting gas, and that the geometry of the medium may well be non-uniform (i.e. clumpy and with a non-uniform sky-covering factor).

4.5.1 The MIR line-emitting region: constraints from line fluxes

The gas density influences line emissivities, so a constraint on n_{H} can be obtained from the observed line fluxes assuming ionization

equilibrium within some radius r . Standard recombination theory connects the rate of Lyman continuum photons, $Q(\text{H}^0)$, i.e. photons with energy $E > 13.6$ eV, to the fluxes of various elemental transitions. A commonly adopted relation between the Balmer line $\text{H}\alpha$ $\lambda 6563$ Å and $Q(\text{H}^0)$ is

$$L(\text{H}\alpha) = 1.36 \times 10^{-12} \times Q(\text{H}^0), \quad (4)$$

where $L(\text{H}\alpha)$ is expressed in erg s^{-1} and $Q(\text{H}^0)$ in photons s^{-1} (cf. Kennicutt 1998; Bouwens et al. 2016). The above relation has only a weak dependence on temperature and abundance.

The dereddened flux of the strong H(6–5) Pf α emission line in MIRI is $F_{\text{H}(6-5)} = 1.1 \times 10^{-12} \text{ erg s}^{-1} \text{ cm}^{-2}$. Uncertainties on this flux are dominated by systematics related to potential confusion with weaker lines and disentangling of the continuum. By experimenting with varying underlying continua and a variety of modelled spectra with NEBULAR, we estimate that these could contribute as much as 25 per cent uncertainty.

The line luminosity in $\text{H}\alpha$ can next be predicted from recombination theory: the typical Case B Pf-to-Balmer line ratio is $\text{Pf}\alpha:\text{H}\alpha \approx 0.0246$ (Hummer & Storey 1987; Schirmer 2016; Chatzikos et al. 2023), which again is not particularly sensitive to the physical conditions over the range inferred above. Together with our systematic uncertainty estimate, we predict $L(\text{H}\alpha) \approx 4.7 (\pm 1.2) \times 10^{35} \text{ erg s}^{-1}$, which, in turn, yields $\log[Q(\text{H}^0)] = 47.5 \pm 0.1$.

Finally, assuming complete ionization equilibrium within some radius r yields the Lyman continuum photon rate as

$$Q(\text{H}^0) = \frac{4}{3} \pi r^3 n_e n_{\text{H}} \alpha_{\text{B}}, \quad (5)$$

where α_{B} is the recombination coefficient and the electron density n_e is taken to be identical to n_{H} . For the inferred temperature constraint (Section 4.2), we expect $\alpha_{\text{B}} \approx 2.5 \times 10^{-13} \text{ cm}^3 \text{ s}^{-1}$ (Osterbrock & Ferland 2006).

A reasonable ansatz for the radius r is the size of the outer accretion disc. At ≈ 200 light-seconds (lt-sec), this is of similar order to our observed time lag (Section 4.4). Adopting this value of r , we finally obtain $n_{\text{H}} \approx 4 \times 10^{10} \text{ cm}^{-3}$ in the MIR emission-line zone.

4.5.2 The MIR line-emitting region: constraints from flux ratios

The relative line strengths, in particular the comparatively weak strength of He II, have constrained the mean temperature of the emission-line region to be $T < 20\,000$ K (Section 4.2).

By contrast, the models in Fig. 9 are not strongly sensitive to space density, with little distinction between spectra up to the maximum densities that can be simulated in NEBULAR, $n_{\text{H}} = 10^8 \text{ cm}^{-3}$. In denser media with $n_{\text{H}} \gtrsim 10^{10} \text{ cm}^{-3}$, the flux ratios of higher-to-lower order transitions of H can change significantly [e.g. the H(9–7):H(7–6) ratio increases by factors of several to exceed unity; Kwan & Fischer 2011; Franceschi et al. 2024], which we do not observe. This places a constraint of $n_{\text{H}} \lesssim 10^{10} \text{ cm}^{-3}$ for the emission-line zone.

This gas density, based upon the observed line *ratios*, is of the same order of magnitude as the n_{H} value inferred from the line *fluxes* in the preceding section, though there is mild disagreement between the two. However, it should be noted that values of $n_{\text{H}} \gtrsim 10^{10} \text{ cm}^{-3}$ or so are relatively high, so the assumption of pure Case B ionization equilibrium that we have relied upon so far may not be valid, with collisional and optical depth effects needing to be accounted for. We will return to this point in Section 4.8.

4.5.3 The MIR continuum-emitting region: a thermal bremsstrahlung origin?

The origin of the MIRI continuum is attributed to physical regions at the system outskirts in several plausible scenarios – either near the outer accretion disc or at the companion star (Rahoui et al. 2010). Our r.m.s. analysis (Fig. 3) also shows a drop in variance at the positions of the emission lines, as expected if the line-emitting gas is not cospatial with (and likely more extended than) the continuum. So, it is instructive to derive estimates of n_{H} for the continuum-emitting gas to compare with the lines.

Here, we focus on the specific scenario of thermal bremsstrahlung radiation from the wind. The wind has been proposed as the obscuring medium in the current obscured state of the source (Miller et al. 2020). Constraints on n_{H} are possible from the MIRI data alone in such a scenario, but we stress that such an origin cannot be definitely proven in our data, though the discussion below will show why it is plausible. Other possible interpretations will be outlined in the following sections. The observed thermal bremsstrahlung flux density can be predicted as (Kellogg, Baldwin & Koch 1975)

$$F_{\nu} = A \sqrt{T} g(\nu, T) e^{-\frac{h\nu}{kT}}. \quad (6)$$

Here, $g(\nu, T)$ is the Gaunt factor of the order of 1 and A is a normalizing factor,

$$A = \frac{2.0 \times 10^{-18} \int n^2 dV}{4\pi d^2}, \quad (7)$$

with all lengths expressed in units of cm, and the constant factor appropriate for flux density in Jy. Here, we utilize the implementation of the bremsstrahlung model in the XSPEC code (Arnaud 1996), with Gaunt factors from the polynomial fits of Karzas & Latter (1961).

The wind must be hot, if launched by the accretion disc, but our data do not provide any constraint on the temperature of the continuum-emitting region, except for the fact that the flat dereddened MIRI spectral energy distribution (SED) implies that the bremsstrahlung spectral cut-off must lie at frequencies higher than the MIR. In such a case, the emission measure ($\int n^2 dV$) is the main parameter governing the normalization of the bremsstrahlung model to the MIRI spectrum. It is then possible to obtain an estimate of the mean wind density, once a characteristic radius is assumed.

Rahoui et al. (2010) used a Compton temperature of $T = 5.8 \times 10^6$ K. However, even much lower values characteristic of the electron temperature in the emission-line region ($T \sim 10^4$ K) change the inferences below by only a factor of ~ 2 . Fitting a bremsstrahlung model to our dereddened MIRI spectrum at $10 \mu\text{m}$, and assuming a mean spherical volume $V = 4/3 \pi r^3$, with r representing the outer disc (200 lt-sec), we find $n_{\text{H}} = (1-3) \times 10^{11} \text{ cm}^{-3}$. One such model is plotted in Fig. 8.

4.5.4 A cross-check from the X-ray absorption column

Finally, a simple consistency cross-check comes from the column density N_{H} estimated from X-ray observations, combined with our estimate of the extent of the obscuring medium:

$$N_{\text{H}} \approx n_{\text{H}} \times r. \quad (8)$$

We do not present X-ray data herein, but the source has clearly faded across the Monitor of All-sky X-ray Image (MAXI) energy range up to ≈ 20 keV, at least (Fig. 1). Previous studies have found Compton-thick columns in the hard state (e.g. Balakrishnan et al. 2021). In early 2023, a column at the *low* end of optical depths

with $N_{\text{H}} = 3 (\pm 0.5) \times 10^{23} \text{ cm}^{-2}$ was reported by Miller & Homan (2023).

Using $r = 200$ lt-sec and a column density of $N_{\text{H}} = 10^{24} \text{ cm}^{-2}$ barely in the Compton-thick regime yields a conservative space density of $n_{\text{H}} \approx 2 \times 10^{11} \text{ cm}^{-3}$. If the space density has a radial profile decreasing away from the nucleus, then n_{H} closer in to the nucleus will be higher. Thus, our estimate should be considered a conservative mean value for a uniformly distributed annular sphere of obscuring matter.

4.6 Summary constraints on gas density and mass

The four separate estimates above yield constraints on the gas density ranging from $n_{\text{H}} \lesssim 10^{10}$ to $4 \times 10^{10} \text{ cm}^{-3}$ in the emission-line region, to $(0.5-2) \times 10^{11} \text{ cm}^{-3}$ inferred from the (MIR and X-ray) continua. These could all arise from the same medium (e.g. the wind), with the difference in densities arising from stratification within the medium. The lower density of the emission-line region is consistent with the lines arising from the diffuse, outer fringes, while the denser, compact zones of the wind could be responsible for the obscuration and the MIR bremsstrahlung emission.

All of these estimates imply that the mass M of this gas surrounding the source must be high. For a uniform spherical distribution of gas,

$$M \approx \frac{4}{3} \pi r^3 n_{\text{H}} m_{\text{p}} f. \quad (9)$$

Taking a filling factor $f = 1$ and $n_{\text{H}} = 10^{10} \text{ cm}^{-3}$ (at the lower end of the above estimates appropriate for the emission-line region), this yields $M \approx 2 \times 10^{22} \text{ kg} = 8 \times 10^{-9} M_{\odot}$.

Alternatively, an outflowing annular shell is likely to be a better description of the geometry of the *wind* known to be present in this source. Assuming $n_{\text{H}} = 10^{11} \text{ cm}^{-3}$ for the bremsstrahlung-emitting wind and a terminal wind velocity $v_{\text{w}} = 10^3 \text{ km s}^{-1}$ (cf. 3000 km s^{-1} was inferred from NIR spectroscopy carried out in May 2023 about 2 weeks prior to the *JWST* observation; Sanchez-Sierras et al. 2023b), we obtain an estimate of the mass-outflow rate as

$$\dot{M} \approx 4\pi r^2 n_{\text{H}} m_{\text{p}} v_{\text{w}} \Omega_{\text{w}} \quad (10)$$

$$= 8 \times 10^{21} \text{ g s}^{-1} = 1 \times 10^{-4} M_{\odot} \text{ yr}^{-1}. \quad (11)$$

This is an extremely high mass-loss rate. Wind covering factors $\Omega_{\text{w}} \ll 1$ could moderate the above rates, but these require a fine-tuned geometry to maintain an obscured view of the source, as has persisted for ≈ 6 yr now since 2018. So, Ω_{w} is unlikely to be very small. A *toroidal* geometry should be dynamically more stable than a sky-covering spheroidal annulus, but such a configuration would still only change \dot{M} by a factor of the order of unity.

The strongest dependence in the mass-loss rate above is on radius ($\dot{M} \propto r^2$), for which we have assumed a plausible size corresponding to the outer disc but we cannot rule out smaller sizes. Reducing r by a factor of 10 (say) would decrease \dot{M} to $\sim 10^{-6} M_{\odot} \text{ yr}^{-1}$ for a constant n_{H} . However, n_{H} should also scale down as r^{-1} (from the X-ray column density estimator; equation 8) or as $r^{-1.5}$ (for a constant bremsstrahlung emission measure; equation 7). So, the dependence of mass-outflow rate on radius is effectively weaker, scaling as $\dot{M} \propto r^{0.5-1}$.

Another inherent assumption is that the wind is unbound. If the MIR continuum probes a phase of the wind distinct from the fast-moving NIR component, v_{w} could also be reduced, thereby

moderating \dot{M} substantially. We will revisit the impact of such assumptions in Section 4.9.

4.7 Other possible sources of the continuum

The MIRI continuum cannot be attributed to the donor star, which should contribute no more than $\lesssim 1$ –10 per cent of the dereddened flux at any wavelength across the MIRI range (cf. Rahoui et al. 2010). The observed flat slope (Fig. 8) is also inconsistent with a simple blackbody.

The outer disc of GRS 1915+105 is approximately 200 lt-sec in radius (cf. Table 1). This is about $(3\text{--}4) \times 10^6$ gravitational radii for the black hole mass $M_{\text{BH}} = 11.2 \pm 1.7 M_{\odot}$. Irradiation by nuclear X-rays and UV can heat the outer disc, flattening its SED relative to a blackbody (e.g. Gierliński, Done & Page 2009). Efficient heating of a large outer disc may then partially account for the shape of the MIRI continuum. It would have to be a very stable outer disc in terms of radiated flux, with an r.m.s. of no more than a few per cent over ≈ 2 h (Fig. 5).

Another possibility is synchrotron radiation. Jetted emission has historically been very strong in this system, and studies of the radio activity during the obscured state have demonstrated continued, enhanced flaring (Motta et al. 2021). If the MIR continuum is dominated by a compact jet, the flat SED requires that the MIR lies in the optically thick regime. This, in turn, constrains the optically thick to thin synchrotron spectral break (ν_b) lying at frequencies higher than the MIRI range, which also places a constraint on the magnetic field (B) at the radiative base of the jet (Blandford & Königl 1979).

To estimate B , we follow the prescription in Gandhi et al. (2011) for a homogeneous single-zone equipartition region at the base of the jet. Taking a lower limit on $\nu_b \geq 7.5 \times 10^{13}$ Hz ($\equiv 4 \mu\text{m}$), a break flux density $F_{\nu_b} \approx 0.13$ Jy (Fig. 9) and a standard optically thick synchrotron spectral slope fall-off $\alpha = -0.7$ ($F_{\nu} \propto \nu^{\alpha}$) yields $B \geq 2 \times 10^4$ G and a zone radius $R \leq 2 \times 10^9$ cm. Similar values have been inferred at the jet base of other systems (e.g. Chaty, Dubus & Raichoor 2011; Gandhi et al. 2011; Russell et al. 2014, 2020; Echiburú-Trujillo et al. 2024), but the lack of secure detection of ν_b precludes more detailed insight and comparison. Similarly to the irradiated disc scenario, our measurement of a weak r.m.s. from the timing data requires the compact jet to be highly stable in flux, which may be difficult to explain given the inferred radius of the jet base above.

Data spanning a wider wavelength coverage will be required to test both the irradiated disc and the jet hypotheses.

4.8 Bolometric luminosity estimates from the MIR

The emission-line analysis above also allows approximate constraints on the ionizing power of the intrinsic source (L_{Bol}). This is because the Lyman continuum photon rate can be written as

$$Q(H^0) = \Omega_{\text{ion}} \int_{\nu_0}^{\infty} \frac{L_{\nu}}{h\nu} d\nu, \quad (12)$$

where $E_0 = h\nu_0 = 13.6$ eV, and Ω_{ion} is the covering factor of the illuminated emission-line gas. If a fraction Ω_w of the sky as seen from the nucleus is obscured by optically thick matter, which blocks the escape of ionizing radiation, then $\Omega_{\text{ion}} = 1 - \Omega_w$.

The intrinsic spectral shape is unknown, especially in the current obscured state of the source. However, using equation (12) above as a ‘bolometric indicator’, it is possible to constrain the source power approximately under different assumptions of the spectral shape.

We illustrate this through two plausible example spectral shapes below.

Using the estimate of $Q(H^0)$ from Section 4.5.1 and assuming a simple power-law model with X-ray photon index $\Gamma = 2$ ($N_E \propto E^{-\Gamma}$, or $L_{\nu} \propto \nu^{-\Gamma+1}$ in equation 12 above) extending over 0.013–100 keV (say), we find $L_{\text{Bol}} \sim 6 \times 10^{37}$ erg s $^{-1}$, where L_{Bol} is taken to closely approximate the ionizing source power. Alternatively, if a multi-colour accretion disc (Mitsuda et al. 1984) with an inner temperature of ≈ 1 keV dominates the intrinsic UV-to-X-ray spectrum (cf. Rahoui et al. 2010), we require $L_{\text{Bol}} \sim 5 \times 10^{38}$ erg s $^{-1}$.

The estimates above provide some first insight on L_{Bol} , as derived from the MIR in the obscured state of GRS 1915+105. Taken at face value, these imply that the intrinsic accretion power could plausibly range over ≈ 5 –30 per cent of L_{Edd} , though there are several important uncertainties to keep in mind.

First, simulations treating the photoionization around the source self-consistently need to be carried out in order to test the viability of the above estimates. A full exploration of the model parameter space – which is highly degenerate in terms of geometry, optical depth, local physical conditions, and the radiation spectrum of the central engine – is well beyond the scope of this work. However, we did conduct preliminary tests using the photoionization code CLOUDY version c23.01 (Chatzikos et al. 2023), by assuming blackbody as well as power-law central ionizing sources with appropriate ionizing photon-rate estimates illuminating spherical or slab gas geometries with density estimates as derived above. Our main finding was that while both a blackbody or a power-law ionizing source can reproduce the flux ratios of the primary emission lines, it is difficult to simultaneously produce the high observed fluxes of the emission lines. Most of our tests fell short in predicted line strength, and required the introduction of additional gas on scales extending to $r \gtrsim 1000$ lt-sec or more to reproduce the observed values. One example acceptable simulation that reproduces the observed fluxes and flux ratios of the brightest H(6–5) and H(7–6) emission lines approximately invokes a 1 keV blackbody (e.g. from an accretion disc) with the ionizing flux as estimated in Section 4.5.1 illuminating a spherical gaseous shell extending over radii between $r = 10^{13}$ and 10^{14} cm. The inner density of the shell is $\log n_{\text{H}} (\text{cm}^{-3}) = 10.5$, and this falls linearly with radius (so the resultant integrated column density is just shy of the Compton-thick regime). If not a numerical artefact, such a physically extended medium may be explained as the left-over ejecta that have accumulated in the circumbinary medium over time, and could also account for the relatively cool temperatures inferred for the MIR emission-line region (cf. Fig. 9). However, we caution that convergent solutions were non-trivial to find and often sensitive to the boundary physical conditions – a sign that optical depth effects at the high densities being simulated likely play a non-trivial role, unsurprisingly. We also found that harder ionizing spectra tended to overproduce the fluxes of He II (and other high-excitation) lines, which we do not observe, with softer spectra instead being preferred.

Another uncertainty is the covering factor Ω_{ion} of the illuminated emission-line gas, which remains unknown. If most lines of sight around the source are heavily obscured, with only a small fraction of the inherent ionizing power escaping out, then Ω_{ion} will be small and L_{bol} will need to be correspondingly boosted upwards. This could be tested by searching for signatures of waste heat emerging in the far-IR or sub-mm regimes.

With the above caveats in the mind, the range of L_{Bol} values herein shows that GRS 1915+105 is at least consistent with the central engine accreting at a moderately high, but sub-Eddington, accretion rate in its present X-ray-obscured state. Detailed validation will be required in future work to test this.

4.9 The origin of the MIR emission of GRS 1915+105

The unique ‘X-ray-obscured’ state of GRS 1915+105 has now lasted for several years. Substantial *radio* flaring has been reported as the X-rays have faded systematically over this time (Motta et al. 2021). Here, we have presented data demonstrating clear *MIR* brightening and flaring, both in terms of the long-term *MIR* monitoring shown in Fig. 1 as well as our pointed *JWST* observation, which caught the source near the peak of one of these long-term *MIR*-flaring periods. This adds to evidence pointing to the presence of an intrinsically active central engine, despite its apparent weakness in X-rays.

The dereddened *MIRI* continuum luminosity of 10^{36} erg s⁻¹ is about 7×10^{-4} of the Eddington power (Section 4.1). Using the emission lines as probes of the intrinsic ionizing power, together with plausible assumptions on the shape of the intrinsic continuum, suggests a bolometric (ionizing) accretion luminosity $L_{\text{Bol}} \approx 5\text{--}30$ percent L_{Edd} (Section 4.8). This is subject to much uncertainty, not only on the spectral shape, but also on the covering factor of the illuminated emission-line nebula, and high L_{Bol} values cannot be ruled out. Nevertheless, such a range is qualitatively consistent with inferences from detailed X-ray studies that the source is accreting at sub-Eddington rates (Miller et al. 2020; Balakrishnan et al. 2021). In any scenario where the *MIR* continuum is dominated by reprocessing of the intrinsic accretion power, the efficiency of reprocessing must then be high: $L_{\text{MIRI}}/L_{\text{Bol}}$ ranges over 0.002–0.02 for the bolometric luminosity range above. When comparing to historical observations with *Spitzer* (Fig. 8), this ratio is now about an order of magnitude higher, presumably as a result of enhanced reprocessing in the circumnuclear gas, which now persistently obscures the central source.

We find a rich *MIRI* recombination line spectrum, which is also much brighter than seen in historical *MIR* spectroscopy before the source entered the obscured state. The *MIRI* spectrum can be approximated as emission from an optically thin shell with mean electron temperature $T < 20\,000$ K (and possibly close to 16 000 K) and gas density $n_{\text{H}} \sim 10^{10}$ cm⁻³ (Section 4.2). The fact that most of the emission lines are less variable (Section 3.2.2) than the continuum is consistent with physically segregated origins of the two. The only exceptions are the two He II lines [(9–8) $\lambda 6.947$ μm and (10–9) $\lambda 9.712$ μm ; cf. Fig. A1], which likely arise closer in to the source of the continuum if helium is to be photoionized.

At first glance, one might interpret the long emission-line lag as the light-travel time to a physically extended gas shell on size scales of \sim few hundred lt-sec. However, given the relatively high densities inferred from our analysis (Section 4.5), it is worth estimating the mean recombination time (τ_{rec}) in the emission-line region. This can be estimated as follows:

$$\tau_{\text{rec}} = \frac{1}{n_{\text{H}}\alpha_{\text{B}}}. \quad (13)$$

For the range of n_{H} values (from $\lesssim 10^{10}$ to $\approx 4 \times 10^{10}$ cm⁻³) estimated in the emission-line region (Section 4.5), τ_{rec} ranges from ≈ 100 to $\gtrsim 400$ s.

These time-scales are similar to those inferred from the emission-line lag analysis, and could partly account for the degeneracy that we inferred between the mean lag τ and smearing length σ when using the Gaussian transfer function (Section 4.4). Radiative transfer effects within dense media could add additional delays. In other words, the lag that we find should not be interpreted solely in terms of a light-travel time delay. It should also be kept in mind that the line response is non-stationary, with the lag itself changing towards the end of our observation (Section 3.2.2). Restricting our

transfer function analysis to the initial 5000 s of the observation results in a characteristic lag $\tau = 60_{-43}^{+76}$ s and smearing parameter $\sigma = 536_{-51}^{+46}$ s. These time-scales are still consistent with the need for a long lag and/or smearing of the emission line as inferred from the full observation (Section 3), though longer duration sampling is needed to quantify these results more accurately.

The *Spitzer* *MIR* spectra were proposed to span a transition (occurring at ≈ 10 μm) between the outer irradiated disc and a cold ($T \sim 300\text{--}500$ K) dust component heated by the companion star (Rahoui et al. 2010). Our results are not easily consistent with such an interpretation, for two reasons: (1) The shape of the observed *MIRI* spectrum is remarkably similar to that seen by *IRS*, despite the source having brightened by a factor of 7–13 in the interim (Fig. 8). Preserving the spectral shape over the years would require fine-tuning to scale up both components identically; (2) If the cold dust component were heated by the companion star, its luminosity would not be expected to differ between the *Spitzer* and *JWST* epochs, leading to a change in spectral shape across the transition, which we do not obviously see. The apparent lack of PAH features in our data (Section 4.3) argues for the dust component to have been heated, and possibly destroyed in the intervening ≈ 17 yr since their detection, by a change in ionizing conditions, which also argues for heating by the compact object instead of the companion star.

In fact, it is non-trivial to preserve the spectral shape in most multicomponent physical scenarios in which the source flux changes dramatically. Instead, a (single-component) power law could achieve this, and the dereddened *MIRI* continuum (Fig. 8) can also be qualitatively explained as an approximately flat power law between 5 and 10 μm (with a slight rise at the blue end below the *Spitzer* *IRS* short wavelength limit, possibly signalling a second component). The source has also shown enhanced radio activity since the 2018 obscured state (Motta et al. 2021), though we cannot say whether any radio power-law synchrotron component extends from the radio to the *MIR* herein. One caveat regarding the modelling of the continuum shape is the apparent spectral calibration uncertainty at both ends of the *MIRI* wavelength range. While we have attempted to correct for these (Appendix A), this needs to be verified and cross-checked against other multiwavelength data.

Interpreting the *MIRI* continuum in terms of thermal bremsstrahlung from the obscuring wind requires a wind density of $n_{\text{H}} \sim 10^{11}$ cm⁻³, about one order of magnitude denser than the emission-line region (Section 4.5). The inferred wind density is also similar to the gas density inferred via X-ray absorption, if this absorbing gas column spans the outer accretion disc. So, the wind could potentially explain the *MIRI* continuum, the *MIR* emission lines (as the outer optically thin fringes of the wind), and could also be the same medium that obscures the X-rays.

While the above scenario may be one self-consistent interpretation of the data, it pushes us into an extreme regime in terms of the strength of matter feedback. At the mass-loss rate required by the wind (Section 4.6), the disc would lose a solar mass in $\approx 10^4$ yr, requiring full replenishment every year (based upon the critical estimates of the disc mass; Koljonen & Hovatta 2021). In terms of the Eddington accretion rate $\dot{M}_{\text{Edd}} = L_{\text{Edd}}/\eta c^2 = 2.6 \times 10^{-7} M_{\odot} \text{ yr}^{-1}$ with standard radiative efficiency $\eta = 0.1$, the source is losing mass at $\approx 10^3 \dot{M}_{\text{Edd}}$. This would clearly be an unsustainable rate for the source to maintain over a long period of time.

The mass-loss could be moderated if the wind speed was itself variable and this is, indeed, observed. An irregular *NIR* wind has been observed on several occasions, with speeds exceeding 10^3 km s⁻¹ (Sánchez-Sierras et al. 2023a). At these speeds, though, the wind cannot remain bound, so such episodes must be transient. Our

JWST observations were conducted very soon after the peak of unprecedented MIR- and radio-flaring activity (cf. Fig. 1), with the source approaching and exceeding radio flux densities of ≈ 1 Jy over Apr–Aug 2023 (Bright et al. 2023; Egron et al. 2023; Trushkin et al. 2023). In other words, the physical parameters that we infer could simply be reflecting the short-lived, albeit extreme, nature of the source state during the past few years. Future MIR observations at more moderate flux levels should be able to easily test this hypothesis.

By contrast, the wind seen in *X-rays* originates closer in to the nucleus and was seen to be an order of magnitude slower at the onset of the obscured state (Miller et al. 2020). In fact, this hot wind may well be a ‘failed outflow’, which does not escape to large scales. If the MIR bremsstrahlung continuum is probing the remnants of such a failed wind, our inferred mass-loss rates would be substantially lowered. Understanding the interplay between the multiple phases of such a wind should be possible through joint X-ray microcalorimeter and MIR high-spectral resolution observations. We also note that we cannot rule out the alternative possibilities of jet or irradiated accretion disc contributions to the MIR continuum (though these also have associated difficulties; Section 4.7), nor have we investigated shock ionization as a mechanism to produce the emission lines observed. Under any of these scenarios, the mass-loss rate would naturally come down, but alternative mechanisms would be required to suppress the expected MIR emission from the excess gas that must be obscuring the source in X-rays.

It is also worth questioning whether GRS 1915+105 is unique among the XRB population in terms of the extreme behaviour described above, and if so, why. The presence of extreme obscuration has been inferred in other well-studied XRBs, e.g. V404 Cyg (Motta et al. 2017; Walton et al. 2017) and Swift J1357.2–0933 (Charles et al. 2019). In the former case, extreme obscuration episodes were short-lived, with the wind clearing the circumnuclear medium in a matter of weeks to months. GRS 1915+105 has a much larger accretion disc than both these systems (and, in fact, has the largest disc of all known Galactic XRBs; Casares & Jonker 2014), affording a much larger reservoir to accumulate gas. The inclination angle of GRS 1915+105 ($i \approx 64$ deg) is also relatively high, so it is easier for gas near the disc plane to cause obscuration along the line of sight (as is thought to be the case in Swift J1357.2–0933). Pinning down the fundamental cause of the transition that resulted in the source entering its current X-ray-obscured state will be key to understanding its relation to other XRBs.

A recent detection of GRS 1915+105 at very high energy gamma-rays could prove instructive in this regard. The Large High Altitude Air Shower Observatory (LHAASO) Collaboration (LHAASO Collaboration 2024) have reported the detection of an extended counterpart to GRS 1915+105 at energies extending up to 100 TeV. Such high energies clearly require the presence of extreme activity in the source, making it an efficient particle accelerator. Hadronic processes within a surrounding large-scale gaseous envelope have been suggested (LHAASO Collaboration 2024). Joint modelling of the MIRI and LHAASO data, together with data at other wavelengths, could put these suggestions to a concrete test.

5 CONCLUSIONS

GRS 1915+105 has brightened dramatically in the MIR compared to historical averages. The now-persistent (X-ray) obscured state is thus characterized by MIR brightening and long-term flaring, in addition to the activity that has been reported in the radio.

MIRI also reveals the presence of a rich emission-line spectrum. Some of the strongest recombination emission lines may have been present in previous *Spitzer* IRS observations, but only at much weaker

S/N, and may have been variable and/or confused with adjacent features (Rahoui et al. 2010; Harrison et al. 2014). Detailed timing analysis in our MIRI data now shows indications of an emission-line lag relative to the underlying continuum. The lag is consistent with time-scales characteristic of the outer accretion disc, and the relatively cool characteristic temperature ($T \lesssim 20\,000$ K) suggests that the emission lines cannot originate very close to the source. However, the lag is also similar to the expected recombination time for its modelled gas density, so cannot be interpreted solely as a light-travel time delay. PAHs apparent in previous data have either remained at a similar strength or may have been destroyed in the interim.

The source is thought to be obscured in X-rays by an optically thick wind. The MIRI continuum could represent optically thick bremsstrahlung emission from such a wind, with the emission lines arising from its outer nebular fringes. This is also commensurate with the integrated column densities inferred from X-ray continuum absorption, and self-consistently explains the lack of any strong flux variations, which would have been washed out in propagating through the optically thick medium.

Using the flux of the most significant MIRI Pf α emission line as a bolometric indicator implies a moderate intrinsic accretion luminosity, though self-consistent photoionization modelling in optically thick media is needed to better constrain this. We are able to constrain the mass of the obscuring medium, but if estimates at the high end of wind speeds are adopted, this would imply an unsustainable rate of mass-loss from the system. *JWST* caught the source during a period of exceptional flaring during 2023, so these extreme inferences need not necessarily apply in the longer term. Irrespective, our analysis adds to evidence arguing that GRS 1915+105 remains active during the ‘obscured’ state, and is perhaps growingly erratic in its multiwavelength behaviour now.

These results not only give new insight into the nature of the unique obscured state of GRS 1915+105, but also showcase possibilities of rapid MIR spectral-timing analysis. *JWST*’s unparalleled sensitivity was crucial for uncovering the weak (~ 1 per cent), but highly significant, r.m.s. that we observe, and for detection of the emission-line lag. We have also highlighted systematic uncertainties that impact current observations in the MIRI LRS spectral-timing mode, and which need to be accounted for when searching subtle features. *JWST* is still a young mission, and better understanding of these systematic issues is expected as knowledge of the MIRI calibration and the reduction pipeline improves with time.

Further work is ongoing to collate and analyse the multiwavelength spectral energy distribution of GRS 1915+105, which should help to test some of the questions raised herein, e.g. on the possibility of jet or irradiated accretion disc contributions to the MIR. Future observations at higher spectral resolution (with *JWST*’s MRS instrument; Wells et al. 2015) will allow superior line deconvolution and searches for wind signatures in the MIR.

ACKNOWLEDGEMENTS

We are grateful to the mission and instrument teams at STScI for their patience and expert help with our numerous queries, especially MIRI scientist S. Kendrew and staff astronomers I. Wong and G. Sloan. We also thank the anonymous referee for their time and their review.

PG acknowledges funding from The Royal Society (SRF\R1\241074). PG and MER thank UKRI Science and Technology Facilities Council (STFC) for support. AJT acknowledges the support of the Natural Sciences and Engineering

Research Council of Canada (NSERC; funding reference number RGPIN-2024-04458). TJM acknowledges support from JWST-GO-01586.002. RIH and ESB acknowledge support from JWST-GO-01586.007. JAT acknowledges support from the Spanish Ministry of Science, Innovation and Universities (MICIU) under grant PID2020-114822GB-I00. JAP acknowledges support from STFC consolidated grant ST/X001075/1. RMP acknowledges support from NASA under award no. 80NSSC23M0104. DDP acknowledges the support from ISRO (India), under the ISRO RESPOND programme. The work of MER was carried out at the Jet Propulsion Laboratory, California Institute of Technology, under a contract with the National Aeronautics and Space Administration. MCB and TDR acknowledge support from the INAF-Astrofit fellowship. GRS and COH were supported by NSERC Discovery Grants RGPIN-2021-0400 and RGPIN-2023-04264, respectively. DMR was supported by Tamken under the NYU Abu Dhabi Research Institute grant CASS. PS-S acknowledges financial support from the Spanish I + D + i Project PID2022-139555NB-I00 (TNO-JWST) and the Severo Ochoa Grant CEX2021-001131-S, both funded by MCIN/AEI. VSD acknowledges support by the Science and Technology Facilities Council (grant ST/V000853/1). SM was supported by a European Research Council (ERC) Synergy Grant ‘BlackHolistic’ grant no. 10107164.

Line identification benefited from the compilation v3.00b4 presented in van Hoof (2018).⁶CLOUDY calculations were performed with version c23.01 (Chatzikos et al. 2023).

This work is based on observations made with the NASA/ESA/CSA *JWST*. The data were obtained from the Mikulski Archive for Space Telescopes at the Space Telescope Science Institute, which is operated by the Association of Universities for Research in Astronomy, Inc., under NASA contract NAS 5-03127 for *JWST*. These observations are associated with programme #1586 (Gandhi et al. 2021). Support for programme #1586 was provided by NASA through a grant from the Space Telescope Science Institute, which is operated by the Association of Universities for Research in Astronomy, Inc., under NASA contract NAS 5-03127.

This research has made use of the NASA/IPAC Infrared Science Archive, which is funded by the National Aeronautics and Space Administration and operated by the California Institute of Technology. The DOI of the *Spitzer* Enhanced IRS Products is 10.26131/IRSA399.

This research has made use of MAXI data provided by RIKEN, JAXA, and the MAXI team.

This research has made use of data and/or software provided by the High Energy Astrophysics Science Archive Research Center (HEASARC), which is a service of the Astrophysics Science Division at NASA/GSFC.

This study is based on observations with *ISO*, an ESA project with instruments funded by ESA Member States (especially the PI countries: France, Germany, the Netherlands, and the United Kingdom) and with the participation of ISAS and NASA.

PG is grateful to G.J.Ferland for help with CLOUDY and to S.F.Hönig, J.Hernandez-Santisteban, and J.H.Matthews for discussions at the initial stages of analysis.

This study is dedicated to the memory of our colleague, Tomaso Belloni.

DATA AVAILABILITY

The core data analysed herein are publicly available in telescope archives. The *JWST* data may be found using the programme identifier 1586 and 1033. The *NEOWISE*, *MAXI*, and *Rossi X-ray Timing Explorer (RXTE)* data are similarly publicly available. AMI data can be made available upon reasonable request to the coauthors.

REFERENCES

- Allamandola L. J., Tielens A. G. G. M., Barker J. R., 1989, *ApJS*, 71, 733
 Argyriou I. et al., 2023, *A&A*, 680, A96
 Armus L. et al., 2023, *ApJ*, 942, L37
 Arnaud K. A., 1996, in Jacoby G. H., Barnes J., eds, ASP Conf. Ser. Vol. 101, Astronomical Data Analysis Software and Systems V. Astron. Soc. Pac., San Francisco, p. 17
 Balakrishnan M., Miller J. M., Reynolds M. T., Kammoun E., Zoghbi A., Tetarenko B. E., 2021, *ApJ*, 909, 41
 Belloni T., 2010, in Belloni T., Lecture Notes in Physics, Vol. 794, The Jet Paradigm. Springer-Verlag, Berlin/ISBN 978-3-540-76936-1
 Belloni T., Hasinger G., 1990, *A&A*, 230, 103
 Belloni T., Klein-Wolt M., Méndez M., van der Klis M., van Paradijs J., 2000, *A&A*, 355, 271
 Blandford R. D., Königl A., 1979, *ApJ*, 232, 34
 Bouwens R. J., Smit R., Labbé I., Franx M., Caruana J., Oesch P., Stefanon M., Rasappu N., 2016, *ApJ*, 831, 176
 Bouwman J. et al., 2023, *PASP*, 135, 038002
 Bradt H. V., Rothschild R. E., Swank J. H., 1993, *A&AS*, 97, 355
 Bright J. et al., 2023, *Astron. Telegram*, 16188, 1
 Casares J., Jonker P. G., 2014, *Space Sci. Rev.*, 183, 223
 Casella P. et al., 2010, *MNRAS*, 404, L21
 Cesarsky C. J. et al., 1996, *A&A*, 315, L32
 Chapuis C., Corbel S., 2004, *A&A*, 414, 659
 Charles P., Matthews J. H., Buckley D. A. H., Gandhi P., Kotze E., Paice J., 2019, *MNRAS*, 489, L47
 Chaty S., Dubus G., Raichoor A., 2011, *A&A*, 529, A3
 Chatzikos M. et al., 2023, *Rev. Mex. Astron. Astrofis.*, 59, 327
 Chiar J. E., Tielens A. G. G. M., 2006, *ApJ*, 637, 774
 Clegg P. E. et al., 1996, *A&A*, 315, L38
 Dyrek A., Ducrot E., Lagage P. O., Tremblin P., Kendrew S., Bouwman J., Bouffet R., 2024, *A&A*, 683, A212
 Echiburú-Trujillo C. et al., 2024, *ApJ*, 962, 116
 Egron E. et al., 2023, *Astron. Telegram*, 16008, 1
 Eikenberry S. S., Matthews K., Morgan E. H., Remillard R. A., Nelson R. W., 1998a, *ApJ*, 494, L61
 Eikenberry S. S., Matthews K., Murphy T. W., Jr, Nelson R. W., Morgan E. H., Remillard R. A., Munro M., 1998b, *ApJ*, 506, L31
 Esquej P. et al., 2014, *ApJ*, 780, 86
 Fender R. P., Pooley G. G., Brocksopp C., Newell S. J., 1997, *MNRAS*, 290, L65
 Fitzpatrick E. L., Massa D., 2009, *ApJ*, 699, 1209
 Foreman-Mackey D. et al., 2019, *J. Open Source Softw.*, 4, 1864
 Franceschi R. et al., 2024, *A&A*, 687, A96
 Fuchs Y., Mirabel I. F., Claret A., 2003, *A&A*, 404, 1011
 Gandhi P. et al., 2008, *MNRAS*, 390, L29
 Gandhi P. et al., 2010, *MNRAS*, 407, 2166
 Gandhi P. et al., 2011, *ApJ*, 740, L13
 Gandhi P. et al., 2016, *MNRAS*, 459, 554
 Gandhi P. et al., 2021, Black Hole Jet Launching Physics with MIRI, *JWST Proposal*. Cycle 1, ID. #1586
 Gierliński M., Done C., Page K., 2009, *MNRAS*, 392, 1106
 Greiner J., Cuby J. G., McCaughrean M. J., Castro-Tirado A. J., Mennickent R. E., 2001, *A&A*, 373, L37
 Harrison T. E., Gelino D. M., Buxton M., Fost T., 2014, *AJ*, 148, 22
 Houck J. R. et al., 2004, *ApJS*, 154, 18
 Hummer D. G., Storey P. J., 1987, *MNRAS*, 224, 801

⁶<https://linelist.pa.uky.edu/newpage/>

- Hynes R. I., O'Brien K., Horne K., Chen W., Haswell C. A., 1998, *MNRAS*, 299, L37
- Hynes R. I. et al., 2003, *MNRAS*, 345, 292
- Karzas W. J., Latter R., 1961, *ApJS*, 6, 167
- Kellogg E., Baldwin J. R., Koch D., 1975, *ApJ*, 199, 299
- Kendrew S. et al., 2015, *PASP*, 127, 623
- Kendrew S. et al., 2018, in Lystrup M., MacEwen H. A., Fazio G. G., Batalha N., Siegler N., Tong E. C., eds, Proc. SPIE Conf. Ser. Vol. 10698, Space Telescopes and Instrumentation 2018: Optical, Infrared, and Millimeter Wave. SPIE, Bellingham, p. 106983U
- Kennicutt R. C. J., 1998, *ARA&A*, 36, 189
- Kessler M. F. et al., 1996, *A&A*, 315, L27
- Koljonen K. I. I., Hovatta T., 2021, *A&A*, 647, A173
- Kwan J., Fischer W., 2011, *MNRAS*, 411, 2383
- Lasso-Cabrera N. M., Eikenberry S. S., 2013, *ApJ*, 775, 82
- Levine A. M., Bradt H., Cui W., Jernigan J. G., Morgan E. H., Remillard R., Shirey R. E., Smith D. A., 1996, *ApJ*, 469, L33
- LHAASO Collaboration, 2024, preprint (arXiv:2410.08988)
- Mainzer A. et al., 2011, *ApJ*, 731, 53
- Malzac J., 2014, *MNRAS*, 443, 299
- Markoff S., Falcke H., Fender R., 2001, *A&A*, 372, L25
- Matsuoka M. et al., 2009, *PASJ*, 61, 999
- Miller J. M., Homan J., 2023, Astron. Telegram, 15908, 1
- Miller J. M. et al., 2020, *ApJ*, 904, 30
- Mirabel I. F., Rodríguez L. F., 1994, *Nature*, 371, 46
- Mirabel I. F., Dhawan V., Chaty S., Rodríguez L. F., Martí J., Robinson C. R., Swank J., Geballe T., 1998, *A&A*, 330, L9
- Mitsuda K. et al., 1984, *PASJ*, 36, 741
- Motta S. E., Kajava J. J. E., Sánchez-Fernández C., Giustini M., Kuulkers E., 2017, *MNRAS*, 468, 981
- Motta S. E. et al., 2021, *MNRAS*, 503, 152
- Muñoz-Darias T., Martínez-Pais I. G., Casares J., Dhillon V. S., Marsh T. R., Cornelisse R., Steeghs D., Charles P. A., 2007, *MNRAS*, 379, 1637
- Negoro H. et al., 2018, Astron. Telegram, 11828, 1
- Neilsen J., Lee J. C., 2009, *Nature*, 458, 481
- Neilsen J., Homan J., Steiner J. F., Marcel G., Cackett E., Remillard R. A., Gendreau K., 2020, *ApJ*, 902, 152
- O'Brien K., Horne K., Hynes R. I., Chen W., Haswell C. A., Still M. D., 2002, *MNRAS*, 334, 426
- Osterbrock D. E., Ferland G. J., 2006, *Astrophysics of Gaseous Nebulae and Active Galactic Nuclei*. University Science Books, Mill Valley, CA
- Paice J. A. et al., 2019, *MNRAS*, 490, L62
- Peterson B. M., 1993, *PASP*, 105, 247
- Predehl P., Schmitt J. H. M. M., 1995, *A&A*, 293, 889
- Rahoui F., Chaty S., Rodríguez J., Fuchs Y., Mirabel I. F., Pooley G. G., 2010, *ApJ*, 715, 1191
- Reid M. J., Miller-Jones J. C. A., 2023, *ApJ*, 959, 85
- Reid M. J., McClintock J. E., Steiner J. F., Steeghs D., Remillard R. A., Dhawan V., Narayan R., 2014, *ApJ*, 796, 2
- Ressler M. E. et al., 2015, *PASP*, 127, 675
- Rieke G. H. et al., 2015, *PASP*, 127, 584
- Rodríguez L. F., Gerard E., Mirabel I. F., Gomez Y., Velazquez A., 1995, *ApJS*, 101, 173
- Rothstein D. M., Eikenberry S. S., Matthews K., 2005, *ApJ*, 626, 991
- Russell T. D., Soria R., Miller-Jones J. C. A., Curran P. A., Markoff S., Russell D. M., Sivakoff G. R., 2014, *MNRAS*, 439, 1390
- Russell T. D. et al., 2020, *MNRAS*, 498, 5772
- Sánchez-Sierras J. et al., 2023a, *A&A*, 680, L16
- Sánchez-Sierras J., Muñoz-Darias T., Motta S., Fender R., Bahramian A., 2023b, Astron. Telegram, 16039, 1
- Schirmer M., 2016, *PASP*, 128, 114001
- Schlafly E. F., Finkbeiner D. P., 2011, *ApJ*, 737, 103
- Shaw A. W. et al., 2025, *AJ*, 169, 21
- Steeghs D., McClintock J. E., Parsons S. G., Reid M. J., Littlefair S., Dhillon V. S., 2013, *ApJ*, 768, 185
- Strong A. W., Mattox J. R., 1996, *A&A*, 308, L21
- Tetarenko A. J. et al., 2021, *MNRAS*, 504, 3862
- Trushkin S. A., Nizhelskij N. A., Tsybulev P. G., Shevchenko A. V., 2023, Astron. Telegram, 15974, 1
- Ueda Y. et al., 2010, *ApJ*, 713, 257
- van der Klis M., Cambridge University Press, Cambridge, 1995, in Lewin W. H. H., van Paradijs J., van den Heuvel E. P. J., eds, *X-ray Binaries*. p. 252
- van Hoof P. A. M., 2018, *Galaxies*, 6, 63
- Vaughan S., Edelson R., Warwick R. S., Uttley P., 2003, *MNRAS*, 345, 1271
- Veledina A., Poutanen J., Vurm I., 2013, *MNRAS*, 430, 3196
- Vincentelli F. M. et al., 2019, *ApJ*, 887, L19
- Vincentelli F. M. et al., 2023, *Nature*, 615, 45
- Voit G. M., 1992, *MNRAS*, 258, 841
- Walton D. J. et al., 2017, *ApJ*, 839, 110
- Wells M. et al., 2015, *PASP*, 127, 646
- Werner M. W. et al., 2004, *ApJS*, 154, 1
- Wright E. L. et al., 2010, *AJ*, 140, 1868
- Wright G. S. et al., 2023, *PASP*, 135, 048003
- Zu Y., Kochanek C. S., Peterson B. M., 2011, *ApJ*, 735, 80
- Zwart J. T. L. et al., 2008, *MNRAS*, 391, 1545

APPENDIX A: COMPARISON WITH ARCHIVAL STELLAR OBSERVATIONS IN THE SLITLESS PRISM TIME-SERIES MODE

During early commissioning, an observation of the bright star, L168–9b, was taken in MIRI SLITLESS PRISM mode in order to calibrate LRS TSOs (Bouwman et al. 2023). L168–9b is known to host a transiting exoplanet, but is otherwise an ordinary M1V star. It is also approximately similar in MIR brightness to GRS 1915+105 at the time of our observation. This commissioning observation thus provides a good comparator in order to assess instrumental systematics.

The commissioning data (Programme ID 1033) were downloaded, reduced, and extracted through the *JWST* pipeline using parameters identical to those adopted for GRS 1915+105. The TSO data in this case comprise 9371 on-sky integrations, each 1.431 s in duration. Detailed analysis of these data can be found in Bouwman et al. (2023) and Dyrek et al. (2024).

The median flux-calibrated spectrum of L168–9b is shown in Fig. A1, together with the spectrum of GRS 1915+105. Some common trends in the continua of both objects are immediately apparent, specifically at the two ends of the wavelength range – at short wavelengths, both spectra have a convex shape between ≈ 4 and $5 \mu\text{m}$ with a steep rise below $4 \mu\text{m}$, while the shape is concave beyond $\approx 12 \mu\text{m}$ where it curves downwards with identical narrow features in both between ≈ 13.5 and $14 \mu\text{m}$. The absolute flux calibration beyond $\approx 12 \mu\text{m}$ is known to be uncertain (e.g. Kendrew et al. 2015), while the shortest wavelength bin at $\approx 3.7 \mu\text{m}$ lies outside the formal MIRI wavelength range. The fact that similar continuum features are seen in both spectra confirms that they must be artefacts of imperfect spectral calibration.

There is a known spectral fold-over at the shortest wavelengths arising from reflection and scattering contamination (Wright et al. 2023), so we do not utilize data below $4.5 \mu\text{m}$ for our science. Above this wavelength, we attempt to correct for the aforementioned imperfections by comparing the MIRI spectrum of L168–9b to a Rayleigh–Jeans (RJ) tail of a blackbody. The flux density in such a tail should scale as $F_\nu \propto \nu^2$. As seen in Fig. A1, L168–9b follows the expected scaling well between ≈ 6 and $8.5 \mu\text{m}$. By normalizing at $8 \mu\text{m}$, we are thus able to correct departures from the RJ tail at both wavelength ends (and all other wavelengths). The assumption here is that the star can be described by RJ. This is not unreasonable for the MIRI range, given that the spectral peak for an M1 star

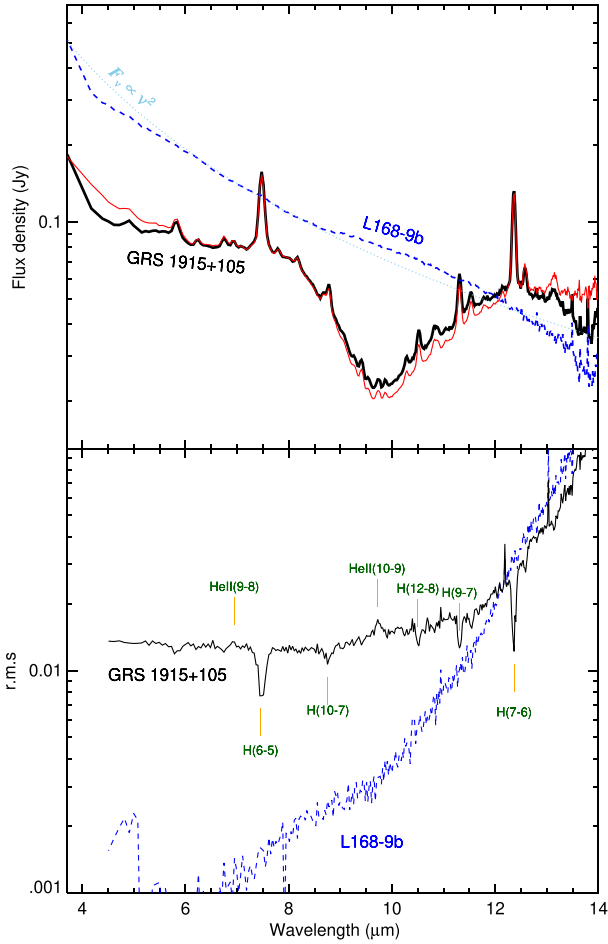


Figure A1. Median spectrum (*top*) and excess r.m.s. (*bottom*) of GRS 1915+105 compared to archival data of the commissioning observation of star L168–9b (blue dashed). In the top panel, the dotted light-blue line shows an expected RJ tail ($F_\nu \propto \nu^{-2}$) normalized to L168–9b at 8 μm , used to determine the residual spectral calibration corrections. The resultant corrected spectrum of GRS 1915+105 is shown in red. In the bottom panel, the wavelengths of prominent emission lines are annotated.

(with effective temperature $T_{\text{eff}} \approx 3600$ K) will lie at a much shorter wavelength around 0.8 μm . However, it does not account for any intrinsic departures, e.g. due to the presence of any dust in the system, and should thus be treated with some caution for precision absolute flux measurements.

With this caveat in mind, applying the RJ correction to our observed spectrum of GRS 1915+105 does result in a smoother continuum at both ends (Fig. A1). Measurement of a more accurate spectral shape will require longer wavelength observations with MIRI/MRS in future cycles, and comparison with NIR spectroscopy, which is beyond the scope of this work. We adopt this correction for our science spectrum presented herein.

The bottom panel of Fig. A1 shows the comparison of the r.m.s. computed according to equation (1) for GRS 1915+105 and L168–9b. The latter star is not expected to be variable in the MIR (except for small systematic flux deviations caused by the exoplanet transit). The rise to the MIR seen in both systems is then clearly an indication of systematics and we thus cannot trust the red continuum r.m.s. rise in GRS 1915+105. A similar discussion can be found in Dyrek et al. (2024), where the rise in r.m.s. is attributed to a diminishing S/N in a

fixed-width extraction aperture at long wavelengths as the spectrum starts to become increasingly background-dominated.

However, the r.m.s. computation (equation 1) should remove any contribution to the variance from the background and other measurement uncertainties. Thus, we do not expect to see any significant r.m.s. in non-variable sources, and the observed r.m.s. trend in Fig. A1 cannot be attributed to diminishing S/N alone. Known issues related to read-noise underestimation could be one of the underlying causes here (see Footnote 1). In consultation with the mission team, we attempted further tests such as cross-checks against the observed variance in the background, but these did not alleviate the issue completely. Future updates to the pipeline should help to resolve this issue, as the mission matures and calibrations improve.

Other than this, L168–9b reassuringly shows much smaller r.m.s. at short wavelengths, implying that our detection of flux variations over the bulk of the MIRI range in GRS 1915+105 is robust.

APPENDIX B: THEORETICAL H AND HE WAVELENGTHS

Table B1 lists the Rydberg series wavelengths of prominent H and He II transitions in the MIRI range. These are listed as a reference to facilitate comparison with the observed spectra.

Table B1. Theoretical wavelengths of some of the most prominent hydrogen series and helium II emission lines in the MIRI wavelength range.

Feature	Wavelength (μm)
Pf (7–5)	4.6538
Pf (6–5)	7.4599
Hp (11–6)	4.6725
Hp (10–6)	5.1286
Hp (9–6)	5.9082
Hp (8–6)	7.5025
Hp (7–6)	12.3719
16–7	5.5252
15–7	5.7115
14–7	5.9568
13–7	6.2919
12–7	6.7720
11–7	7.5081
10–7	8.7600
9–7	11.3087
16–8	7.7804
15–8	8.1549
14–8	8.6645
13–8	9.3920
12–8	10.5035
11–8	12.3871
17–9	10.2612
16–9	10.8036
15–9	11.5395
14–9	12.5870
20–10	12.1568
19–10	12.6109
18–10	13.1880
17–10	13.9417
He II (8–7)	4.7635
He II (9–8)	6.9480
He II (10–9)	9.7135
He II (11–10)	13.1283

Table C1. Multiwavelength extinction towards GRS 1915+105.

λ (μm)	A_λ (mag)
0.55	19.60
1	7.99
2	2.41
3	1.39
4	1.06
5	0.91
6	0.84
7	0.82
8	0.84
9	1.52
10	2.12
11	1.66
12	1.31
13	1.14
14	1.16
15	1.22
16	1.29
17	1.38
18	1.47
19	1.52
20	1.48
21	1.40
22	1.31
23	1.24
24	1.16
25	1.09
26	1.03
27	0.97

APPENDIX C: EXTINCTION CURVE FOR GRS 1915+105

Table C1 lists the values of extinction A_λ spanning the optical to MIR towards GRS 1915+105 used herein. This assumes an $A_V = 19.6 \pm 1.7$ mag (Chapuis & Corbel 2004), combined with the IR extinction curves of Fitzpatrick & Massa (2009) and Chiar & Tielens (2006).

¹School of Physics & Astronomy, University of Southampton, Southampton SO17 1BJ, UK

²Department of Physics & Astronomy, Louisiana State University, 202 Nicholson Hall, Baton Rouge, LA 70803, USA

³Department of Physics & Astronomy, Texas Tech University, Box 41051, Lubbock, TX 79409–1051, USA

⁴Department of Physics and Astronomy, Butler University, 4600 Sunset Avenue, Indianapolis, IN 46208, USA

⁵Cahill Center for Astronomy & Astrophysics, California Institute of Technology, Pasadena, CA 91125, USA

⁶INAF-Osservatorio Astronomico di Brera, Via Bianchi 46, I-23807 Merate (LC), Italy

⁷Department of Astronomy and Astrophysics, Tata Institute of Fundamental Research, 1 Homi Bhabha Road, Colaba, Mumbai 400005, India

⁸Space Telescope Science Institute, 3700 San Martin Drive, Baltimore, MD 21218, USA

⁹South African Astronomical Observatory, P.O. Box 9, Observatory, 7935, South Africa

¹⁰INAF-Osservatorio Astronomico di Roma, via Frascati 33, I-00078 Monteporzio Catone (RM), Italy

¹¹Department of Physics, University of Warwick, Gibbet Hill Road, Coventry CV4 7AL, UK

¹²Astrophysics, Department of Physics, University of Oxford, Keble Road, Oxford OX1 3RH, UK

¹³European Southern Observatory, Alonso de Córdova 3107, Casilla 19001, Vitacura, Santiago, Chile

¹⁴Department of Physics and Astronomy, University of Sheffield, Sheffield S3 7RH, UK

¹⁵Instituto de Astrofísica de Canarias, E-38205 La Laguna, Tenerife, Spain

¹⁶Department of Physics, University of Alberta, CCIS 4–181, Edmonton, AB T6G 2E1, Canada

¹⁷Anton Pannekoek Institute for Astronomy & Gravitation Astroparticle Physics Amsterdam (GRAPPA) Institute, University of Amsterdam, Science Park 904, NL-1098XH Amsterdam, the Netherlands

¹⁸Dipartimento di Fisica, Università degli Studi di Milano, Via Celoria 16, I-20133 Milano, Italy

¹⁹Harvard-Smithsonian Center for Astrophysics, 60 Garden Street, Cambridge, MA 02138, USA

²⁰Department of Astronomy, University of Michigan, 1085 South University Avenue, Ann Arbor, MI 48109, USA

²¹ICRAR – Curtin University, GPO Box U1987, Perth, WA 6845, Australia

²²Centre for Extragalactic Astronomy, Department of Physics, Durham University, South Road, Durham DH1 3LE, UK

²³Department of Physics, R. J. College, Mumbai 400086, India

²⁴Department of Physics, University of Nevada, Reno, NV 89557, USA

²⁵Department of Physics & Astronomy, Embry-Riddle Aeronautical University, 3700 Willow Creek Road, Prescott, AZ 86301, USA

²⁶Jet Propulsion Laboratory, California Institute of Technology, 4800 Oak Grove Drive, Pasadena, CA 91109, USA

²⁷Center for Astrophysics and Space Science (CASS), New York University Abu Dhabi, PO Box 129188, Abu Dhabi, UAE

²⁸INAF – IASF Palermo, via Ugo La Malfa, 153, I-90146 Palermo, Italy

²⁹Instituto de Astrofísica de Andalucía (CSIC), Glorieta de la Astronomía s/n, E-18008 Granada, Spain

³⁰Departamento de Astrofísica, Universidad de La Laguna, E-38206 La Laguna, Tenerife, Spain

³¹Department of Physics and Astronomy, University of Lethbridge, Lethbridge, AB T1K 3M4, Canada

³²Space Sciences Laboratory, University of California, 7 Gauss Way, Berkeley, CA 94720–7450, USA

This paper has been typeset from a $\text{\TeX}/\text{\LaTeX}$ file prepared by the author.